RESEARCH ARTICLE | MARCH 12 2025

Effects of fluid ice content and bed wetness on entrainment of debris flows induced by ice avalanches

Xiangning Li ; Jiangang Chen ; Xiaoqing Chen ; Xi'an Wang; Jinshui Wang; Hechun Ruan; Min Huang

Physics of Fluids 37, 036617 (2025)
https://doi.org/10.1063/5.0256049

Physics of Fluids ARTICLE pubs.aip.org/aip/pof

Effects of fluid ice content and bed wetness on entrainment of debris flows induced by ice avalanches

Cite as: Phys. Fluids **37**, 036617 (2025); doi: 10.1063/5.0256049
Submitted: 2 January 2025 · Accepted: 19 February 2025 ·
Published Online: 12 March 2025

Xiangning Li,[1,2,a] Jiangang Chen,[1,2,b] Xiaoqing Chen,[1,2,c] Xi'an Wang,[1,2,d] Jinshui Wang,[1,2,e] Hechun Ruan,[1,2,f] and Min Huang[1,2,g]

AFFILIATIONS

[1]Key Laboratory of Mountain Hazards and Earth Surface Process, Institute of Mountain Hazards and Environment, Chinese Academy of Sciences (CAS), Chengdu 610041, China
[2]University of Chinese Academy Sciences, Beijing 100049, China

[a)]Electronic mail: lixiangning@imde.ac.cn
[b)]Author to whom correspondence should be addressed: chenjg@imde.ac.cn
[c)]Electronic mail: xqchen@imde.ac.cn
[d)]Electronic mail: wangxian@imde.ac.cn
[e)]Electronic mail: wangjs@imde.ac.cn
[f)]Electronic mail: ruanhechun@imde.ac.cn
[g)]Electronic mail: minhuang@imde.ac.cn

ABSTRACT

Debris flows induced by ice avalanches (*DFIs*) are unique glacial debris flows formed by ice melt during the movement of a rock-ice avalanche. *DFIs* consist of ice, water, and soil. *DFIs* occur frequently in alpine regions worldwide. Soil bed erosion is perhaps the most important momentum exchange process controlling the destructive potential of debris flows. To mitigate *DFI* hazards, erosion characteristics must be studied in depth. However, the effect of ice in fluids on the erosion process has yet to be elucidated. Bed sediments in nature are rarely saturated or fully dry, especially considering that *DFIs* occur during rainfall and the infiltration of ice melt water. The existing erosion theories have adopted saturated soil mechanics to describe the failure of bed soil. This study investigated the influence of ice in fluids and the water content of bed soil on entrainment by a *DFI* on the basis of flume tests. The results showed that the flow charge after erosion was greater than that before erosion, with an increase ranging from 34.48% to 84.21%. This demonstrated that the mobility of the *DFI* was significantly enhanced after erosion. The erosion depth showed fluctuating variations. A_{me} increased and then decreased with increasing ice content. There was no significant linear correlation with the water content of the bed soil. The maximum pore pressure in unsaturated bed soil showed positive feedback with erosion. Based on the analysis of the contribution of collisional stresses to erosion, an erosion model for *DFIs* was eventually proposed.

I. INTRODUCTION

Debris flows induced by ice avalanches (*DFIs*) are a type of glacial debris flow with many occurrences worldwide. It can be formed by the transformation of the movement of rock-ice avalanches. *DFIs* are formed when ice melts during the movement of rock-ice avalanches (Evans *et al.* 2009) or by the breach of the obstruction formed when moraines near a glacier are blocked by rock-ice avalanches (Wei *et al.*, 2018; Wang *et al.*, 2021). Following the work of Guo *et al.* (2023), Peng *et al.* (2022), and Wang *et al.* (2023), an amount of ice proportional to the solid material is contained in a *DFI*. Therefore, a *DFI* is a three-phase flow that has different characteristics from debris flows caused by glacial lake outbursts (Allen *et al.*, 2016), glacial debris flows (Chiarle *et al.*, 2007), and rainfall debris flows. However, the kinematics and erosion mechanisms of *DFIs* remain unclear.

When the shear stress imposed by a debris flow on the bed soil exceeds the resistance exerted by the bed, it leads to erosion (Pudasaini, 2012). Bed sediment entrainment has been investigated based on field and laboratory studies. Several erosion models have

been derived. Two basic types of erosion models include empirical and mechanical models. Empirical models are derived based on the characteristics of debris flow movement. McDougall and Hungr (2005) assumed that the increase in the volume of a debris flow with displacement during its movement follows an exponential function. The erosion rate model is therefore a simplified model based on a growth factor. Other empirical erosion models have been developed in terms of the material concentration (Shieh *et al.*, 1996), stream power (Whipple and Tucker, 1999), yield stress, and relative density changes of debris flows (Chen and Zhang, 2015). The shear stress exerted by a debris flow can be calculated by the model of the steady stream. The Mohr–Coulomb failure criterion can be used to develop the resistance forces of bed sediment (Han *et al.*, 2015; Han *et al.*, 2018). Derived erosion models of debris flows can be divided into single-phase and two-phase models. The upper debris flow was regarded as a single-phase flow in the single-phase model, and the eroding force of debris flow mixture is determined by its rheological behavior (Li *et al.* 2024). The solid and fluid phases and the strong interactions between the phases, including drag and viscous effects, were considered in the two-phase erosion model. The total erosion rate comprises two aspects: the solid erosion rate and the fluid erosion rate (Pudasaini and Fischer, 2020). Based on the two-phase model, the multiphase models considering the phases of the coarse solid fraction, fine solid fraction, and viscous fluid were proposed (Pudasaini and Mergili, 2019). For the extensive erosion velocities, unified mechanical erosion rates, and the advanced net momentum productions into the mass and momentum balance equations, a multi-phase model is developed. It makes a complete description of multi-phase erosive dynamics. Currently, debris flow erosion models for rainfall debris flows and glacial debris flows in alpine regions, especially the *DFI*, are lacking. The role of ice during the *DFI* erosion process has been simulated (Peng *et al.*, 2022; Wang *et al.*, 2023). A *DFI* erosion model that explicitly reflects the role of ice has not been developed, nor has it been derived based on experiments.

The entrainment of debris flows depends on the properties of the fluid and bed soil (Roelofs *et al.*, 2022; Roelofs *et al.*, 2023). The properties of the fluid mainly depend on the composition of the debris flow material and the velocity (Li *et al.*, 2021). The properties of the bed soil are influenced mainly by its particle composition, particle content, and shape (Li *et al.*, 2022; Roelofs *et al.*, 2023). In these studies, the bed soil is generally considered dry or saturated. However, natural channel beds are unsaturated when debris flows occur (Ng *et al.*, 2022; Song and Choi, 2021). The water content of the bed sediment has a significant influence on the erosion characteristics of the debris flows. According to the work of Iverson *et al.* (2011), the water content of the bed soil has a positive feedback effect on the erosion characteristics of the debris flow and further enhances its mobility. The difference between rock-ice avalanches and a general debris flow is the presence of the ice in it. To investigate the erosion characteristics of *DFI*, it is necessary to examine the effect of fluid ice content and bed conditions on erosion. Miniaturized flume experiments are a popular method that can provide a clear representation of the movement of debris flow (Cui *et al.*, 2015). Therefore, the erosion characteristics of *DFI* were analyzed based on the flume experiments.

This paper is organized as follows: The instrumentation, test program, and procedure used in the experiment are introduced in Sec. II. Section III investigates the changes in the velocity, flow depth, and erosion depth with different ice contents in the *DFI*. Section IV discusses the role of ice and the impact of the ice content of the *DFI* and the water content of bed soils on the erosion. Finally, conclusions are drawn in Sec. V.

II. PHYSICAL MODELING OF THE EROSION OF AN UNSATURATED SOIL BED VIA a *DFI*

A. Scaling considerations

In this study, flume experiments were conducted to determine the effects of ice content and bed water content on erosion of *DFI*. Similitude between model and prototype flows is difficult to achieve in most physical experiments. The Froude number *Fr*, which characterizes the relative importance of the flow inertial and gravitational forces, was used to analyze the motion characteristics of the *DFI* to determine the effect of the experimental scale of the model on the experimental results. It is given as follows (Song *et al.*, 2021):

$$Fr = \frac{v}{\sqrt{gh\cos\theta}}, \tag{1}$$

where v is the flow velocity of the *DFI* (m/s); h is the flow depth (m); θ is the slope inclination (°); and g is the gravitational acceleration. The Froude number in the field ranges from 0.5 to 7.6 (Choi *et al.*, 2015). Several preliminary experiments were conducted to determine the appropriate Froude number of the *DFI* prior to the formal experiments. The Froude number ranges between 2.2 and 6.4 in this paper, which is consistent with the movement characteristics of prototype flows in the field.

B. Experimental setup

The flume consisted of a tank, a straight rectangular channel, and a tailing pool (Fig. 1). The flume was 4 m in length, including 2 m long and 0.5 m long non-erodible sections, followed by a 1.5 m long erodible section between the two non-erodible sections. The bed material was placed in the erodible section, which was designed to be 0.12 m deep to ensure adequate room for erosion. The height of the flume was 0.4 m. The sidewall was made of transparent tempered glass, allowing the erosion process to be observed and the velocity to be measured. The flume was fixed at an angle of 18° to the horizontal plane. This was determined based on the critical conditions for the occurrence of *DFIs* in Tianmo gully. The mean slope of Tianmo gully is 16°. Erosion occurred on gradients of 15°–21° (Breien *et al.*, 2008). Therefore, the channel slope of the flume was defined as 18°.

The flume bed was made of a stainless steel plate of 5 mm thickness. Three pairs of circular holes of different diameters are arranged in the flume, allowing a triaxial load cell (LH-SZ-02, capacity:100N and accuracy: 0.01N) and pore pressure transducer (PPT, JUL-P31, capacity: 10 kPa and accuracy: ±0.1% F.S.) to be installed in each pair. The diameters of the holes reserved for mounting the triaxial load cell and pore pressure transducer were 63 and 10 mm, respectively. The distance between the centers of these circular holes was 66.5 mm. In the upstream area of the flume, the circular hole for installing the triaxial load cell was 0.2 m from the erodible section. In the middle of the flume, the distance between the circular hole for installing the triaxial load cell and the upstream erodible section was 0.8 m, and the lowermost circular hole for installing the triaxial load cell was 231.5 mm from the bottom of the flume.

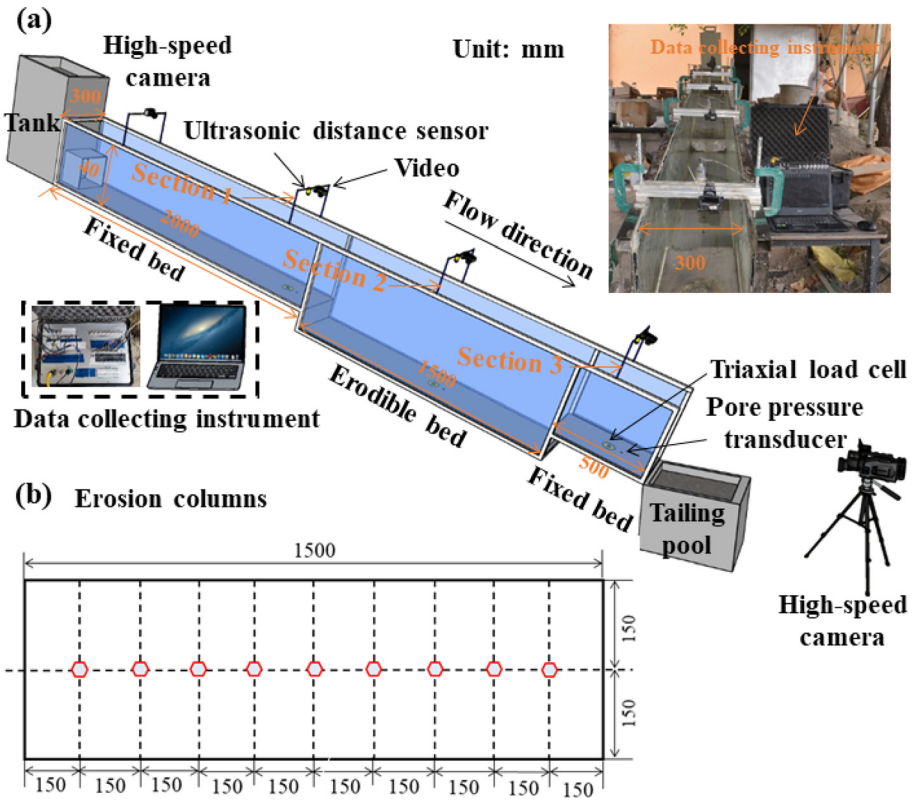

FIG. 1. Schematic diagram of the experimental apparatus. (a) Flume setup and instruments and (b) plan layout of the erosion columns. All dimensions are in millimeters.

C. Instrumentation and measurement

The instrumentation layout is shown in Fig. 1(a). The tank was located at the uppermost part of the flume. The tailing pool was placed at the bottom of the flume to collect the debris flow material. Three monitoring sections were located in the flume. The same types of instruments were placed in each section, including a triaxial load cell, a PPT, ultrasonic sensors (U-GAGE T30UX, accuracy: 0.1 mm), and a high-speed video camera (GoPro hero black 7; 120 fps). The movement of *DFI* was measured by the high-speed camera (SONY FDR-AX60, accuracy: 120 fps) in front of the flume. The data from the sensors were collected using a data collection instrument [Fig. 1(a)]. It has a sampling frequency of 500 Hz to ensure data accuracy. The normal and shear stresses at the flume were measured using a triaxial load cell. The pore fluid pressure was detected using PPT. When the sensors were mounted, the triaxial load cell was coupled with a circular force plate 6 cm in diameter. The gap between the circular hole and force plate was covered with a thin coating to ensure the reliable measurement of shear stress. The open end of the PPT was threaded and was screwed directly into the reserved 5-mm-wide circular hole in the flume. The open end of the PPT was covered by a 2 mm steel mesh, which isolated the pressure induced by the solid phase. The open end of the PPT was filled with silicone oil to effectively transmit the pressure of the fluid phase.

Ultrasonic sensors was mounted along the centerline of the flume directly above the triaxial load cell to capture the flow depth in each section. The small high-speed video camera was placed to the side of the ultrasonic sensor, and the photographs were used to calculate the velocity and analyze the debris flow movement characteristics.

Erosion columns, which have similar working principles to those of erosion sensors (Ng *et al.*, 2022; Song and Choi, 2021), were adopted to measure the entrainment depth. Nine erosion columns were constructed at the centerline of the erodible section. Thirty nuts with inner and outer diameters of 3 and 7 mm, respectively, and a nut with a mass of approximately 0.8 g were included in each erosion column. The nuts were threaded through 0.2-m-long rods that were removed from the base of the erodible section. The columns of nuts were initially prepared to achieve the same height as the initial elevation of the erodible bed. The bed material was then prepared. Afterward, the rods were removed without disturbing the nut columns or the bed material. The nine erosion columns were installed along the centerline of the channel at distances of $l = 0.15$, 0.30, 0.45, 0.60, 0.75, 0.90, 1.05, 1.20, and 1.35 m from the interface between the non-erodible and erodible beds [Fig. 1(b)]. During each test, the nuts near the surface of the erodible bed were carried away along with the bed material. The erosion depth was deduced from the difference in the height of the columns before and after the test, which was further used for calculating the erosion rate in this study.

D. Material

The erosion process of the simulated *DFI* along the channel was analyzed in this study. The debris flow material used in the experiment was collected from a typical area to ensure that the results would be representative. Many destructive rock-ice avalanches and subsequent

glacial debris flows have occurred in the Tianmo gully on the southeastern Tibetan Plateau (Ge *et al.*, 2014; Guo *et al.*, 2023; and Wang *et al.*, 2022b). Large-scale debris flows in this area were frequent and have recently occurred, and ice blocks sometimes existed in these areas (Gao *et al.* 2019). The region has become an important area for the study of glacial debris flows. Undisturbed samples were therefore obtained from the deposition area of Tianmo gully for the experimental.

In general, the width of a flume should not be less than five times the maximum particle size of the test materials to account for boundary effects (Cui *et al.*, 2015). Accordingly, a maximum test material particle size of 20 mm was selected for the experiment. The grain size distribution of the test material was measured through sieving and the Bettersize 2000 laser particle size analyzer (Fig. 2). The median particle size was 0.81 mm. The coefficient of uniformity was 63.00, and the coefficient of curvature was 1.29. The soil samples is the widely graded sediment with 39.14% gravel, 43.37% sand, 16.01% silt, and 1.48% clay by volume. The glacial till is dominated by large particles at Tianmo gully. The average particle density was used as the density of the solid phase ρ_r, which is 2760 kg/m^3 (Zhou *et al.* 2019). A 0.05 m^3 *DFI* mixture was used in this study.

According to the work of Wang *et al.* (2022a) and Yang *et al.* (2019), in experiments, the size of an ice fragment should be consistent with the maximum particle size of the debris flow mixture. Accordingly, a uniform ice cube size of $20 \times 20 \times 20$ mm^3 was chosen for this study. The phenomenon and influence of the related phase transitions with the generation of meltwater were negligible. The reason is that the ice essentially does not melt within shorter debris flow distances, so the phase transition plays only a minor role (Wang *et al.*, 2022a; Wang *et al.*, 2023; and Yang *et al.*, 2019). The density of the ice was 920 kg/m^3. The volumes of the *DFI* mixture and ice cubes were kept consistent throughout the experiment. The ice content was determined based on the volume ratio of ice to debris flow mixture. Zhou *et al.* (2024) statistically concluded that the ice content in natural rock-ice avalanche events was generally 20%–60%. *DFIs* were formed when the ice melts during the movement of rock-ice avalanche. Therefore, this can conclude that the ice content in *DFI* is significantly lower than that in rock-ice avalanche, especially as they move to the outlet of the gully. Following the working of Wang *et al.* (2023), water and ice together accounted for 40% of the initial landslide materials at the Zelunglung catchment. The ice content of the released glacial deposit was around 13% when rock-ice avalanches moved to the mouth of the catchment. Considering the experimental costs, the maximum ice content was determined to be 20% in this study. Groups of flows with ice contents of 0%, 5%, 10%, 15%, and 20% were employed. This depends on the volume ratio of ice and the two-phase mixture.

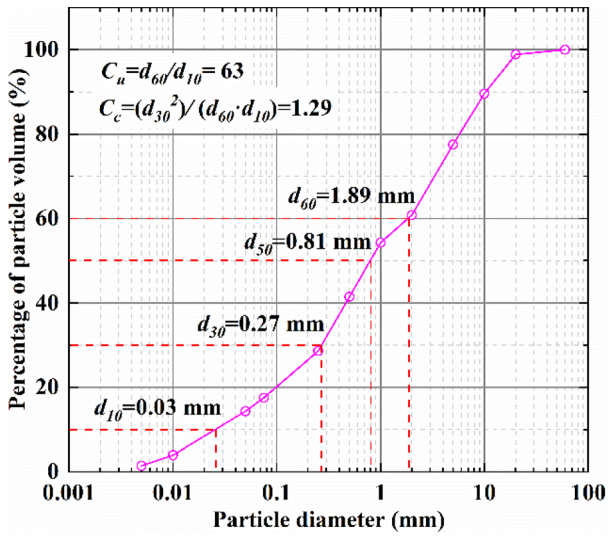

FIG. 2. The particle size distribution of the debris flow at Tianmo gully.

The erodible bed has the same grain size composition as the *DFI* mixture. The loose sediments were placed on the erodible bed. Bed sediments with different water contents were prepared for hand preparation. The tests were carried out 24 h after the preparation of the erodible bed to ensure a uniform bed water content. The water content of the erodible bed w was varied from 0% to 14%, corresponding to initial matric suctions from 22.0 to 11.1 kPa. Table I shows the measured geotechnical properties of the bed sediments.

E. Test program and procedure

The volumetric solid concentration of the two-phase mixture was set to 0.3. The ice content of the *DFI* and the water content of the bed sediment were changed for different experiments, resulting in five ice contents and six water contents. In total, 30 tests were conducted. The test program is summarized in Table II. All the sensors and high-speed cameras were placed at their specific locations in the flume prior to experimentation. The sensors were connected to a data collection instrument to measure real-time data. The preparation of the *DFI* mixture and filling of the bed sediment were then carried out. The bed sediment with a specific water content was placed inside the channel to occupy a mold with dimensions of $1500 \times 300 \times 120$ mm^3 in a loose state. The erosion columns were buried in the sediment during this process. After the bed sediment was prepared, the rods were removed vertically without disturbing the column of nuts or the erodible bed.

In the experiment, the high-speed cameras and data collection instrument were turned on. The two-phase materials were mixed in a flume storage container to ensure that were uniformly mixed, after which the ice cubes were poured into the container. This case simulated the failure of a rock mass overlain by a glacier, after which a debris flow was initiated. The flow was initiated by lifting the container gate after waiting for five seconds. The sensors and data collection instrument were turned off, and the experiment was stopped when the *DFI* materials flowed into the tailings pool. Each group of experiments was completed within 10 s to reduce the melting of the ice. During the experiments, the white plastic balls with a diameter of 20 mm and the density much less than that of water, ice, and *DFI* were thrown into the flume. It has no effect on the motion characteristics of the *DFI*, and it can move with the *DFI* due to its low density and mass. The movement of the balls was recorded by the high-speed camera. By analyzing the video frame by frame, the movement time of the white plastic ball at a certain distance can be obtained. Then, the frontal velocity of the *DFI* was determined.

DFIs generally occur during warmer seasons, and the temperature are within the range of 10–25 °C (Wei *et al.*, 2018). Therefore, the experiments were conducted at room temperature to remain the natural environment.

TABLE I. Summary of the experimental program and bed properties.

	Bed material properties			
Test ID	Degree of saturation, *Sr.*,	Water content, *w*	Initial matric suction, $(u_a\text{-}u_w)_0$ (kPa)	Internal friction angle, φ (°)
_1	0.00	0.00	...	29.6
_2	0.06	0.05	22.0	32.3
_3	0.10	0.08	13.0	34.4
_4	0.13	0.10	12.1	35.6
_5	0.17	0.12	11.1	36.0
_6	0.21	0.14	10.0	41.5

TABLE II. Summary of the test results. The locations of section 1, section 2, and section 3 are shown in Fig. 1. The average erosion depth was the average of the erosion depths measured by each erosion column. The average erosion rate defined as the ratio of the average erosion depth and the erosion time, which was the time required for the *DFI* to move the whole bed.

	Section 1			Section 2			Section 3				
Test ID	Velocity (m/s)	Flow depth (m)	*Fr*	Velocity (m/s)	Flow depth (m)	*Fr*	Velocity (m/s)	Flow depth (m)	*Fr*	Average erosion depth (mm)	Average erosion rate *E* (mm/s)
A11	2.92	0.039	4.84	2.97	0.056	4.11	3.23	0.043	5.10	40.33	96.03
A12	2.46	0.036	4.24	3.14	0.042	5.02	2.89	0.042	4.62	27.00	84.38
A13	2.64	0.037	4.49	2.75	0.039	4.56	3.79	0.039	6.28	26.67	63.49
A14	2.52	0.037	4.29	2.89	0.037	4.92	3.14	0.038	5.27	28.33	64.39
A15	2.46	0.035	4.31	2.75	0.030	5.20	3.14	0.044	4.90	30.00	75.00
A16	2.64	0.036	4.56	2.97	0.039	4.92	3.14	0.038	5.27	37.00	66.07
B11	1.97	0.043	3.11	3.05	0.053	4.34	2.44	0.045	3.77	40.33	56.02
B12	1.80	0.038	3.02	2.82	0.040	4.62	2.44	0.048	3.65	26.33	59.85
B13	1.80	0.035	3.15	2.89	0.035	4.56	3.14	0.044	4.90	33.00	75.00
B14	1.80	0.035	3.15	3.05	0.038	5.12	2.75	0.043	4.34	33.33	69.44
B15	1.80	0.033	3.24	3.05	0.048	4.56	3.14	0.042	5.02	34.00	77.27
B16	1.66	0.039	2.75	2.97	0.042	4.74	2.75	0.043	4.34	34.33	85.83
C11	1.8	0.040	4.42	3.05	0.040	4.99	3.66	0.047	5.53	40.00	100.00
C12	1.8	0.035	4.62	2.97	0.035	5.20	2.75	0.038	4.62	29.33	66.67
C13	1.8	0.045	4.17	3.14	0.050	5.94	2.44	0.050	3.57	29.33	66.67
C14	1.44	0.045	4.40	3.05	0.028	5.97	2.33	0.038	3.68	27.33	62.12
C15	2.70	0.035	4.73	3.05	0.040	4.99	3.79	0.038	6.37	34.67	78.79
C16	2.70	0.037	4.60	2.89	0.040	4.73	3.05	0.041	4.93	33.33	75.76
D11	1.8	0.049	2.66	3.05	0.047	4.61	3.14	0.044	4.90	33.33	69.44
D12	1.97	0.033	3.55	3.14	0.039	5.21	3.66	0.040	5.99	31.33	71.21
D13	1.80	0.037	3.06	2.75	0.039	5.69	2.75	0.038	4.62	32.33	73.48
D14	1.80	0.033	3.24	3.14	0.027	6.26	2.44	0.036	4.21	31.33	71.21
D15	1.97	0.034	3.50	2.89	0.028	5.65	3.14	0.045	4.85	32.00	72.73
D16	1.66	0.043	2.62	2.65	0.031	4.93	2.20	0.040	3.60	19.67	49.17
E11	1.66	0.040	2.72	2.97	0.040	4.86	2.44	0.043	3.85	43.33	98.48
E12	1.44	0.045	2.22	3.05	0.039	5.06	2.44	0.045	3.77	24.00	54.55
E13	1.80	0.038	3.02	2.44	0.034	3.99	2.75	0.040	4.50	23.33	53.03
E14	1.55	0.037	2.64	2.44	0.038	4.10	3.14	0.036	5.42	19.67	40.97
E15	1.55	0.039	2.57	2.89	0.036	4.99	2.75	0.050	4.03	27.67	62.88
E16	1.97	0.036	3.40	3.14	0.040	5.14	3.14	0.040	5.14	32.67	74.24

III. RESULTS AND INTERPRETATION

A. Erosion process

Figure 3 shows the observed erosion process. When the *DFI* propagated to the top of the bed sediment, the liquid material first seeped into the bed soil. A potential saturated distinct will be formed, and erosion occurred within this region. Erosion and fluid infiltration occurred simultaneously. As the subsequent fluids propagate over the bed soil, the liquid material gradually stops infiltrating the soil at the upstream location of the erodible bed. The bed soil height becomes lower than the initial height after the bed soil is entrained.

A significant collision occurs in the middle section of the bed, where the *DFI* interacts with the bed surface. The *DFI* propagates by ascending and moving erratically, thereby entraining the bed soil. The ice contained within the *DFI* moves along as it propagates. A significant amount of ice can be observed at the front of the *DFI* [Fig. 4(a)].

The three erosion patterns were defined in a previous study (McCoy *et al.*, 2012): progressive grain-by-grain erosion, progressive failure with slab-by-slab entrainment, and en-masse failures. Ng *et al.* (2022) reported that three erosion patterns were observed. The observed erosion patterns were consistent with the findings of Song *et al.* (2024). The erosion pattern of en-masse failure was observed in this study [Fig. 4(b)]. The most erosion occurred near the transition from the non-erodible to the erodible section. A similar spatial erosion pattern was observed by Song and Choi (2021) and Haas and Woerkom. (2016). This is attributed to the protective effects of the deposition layer downstream of the erodible bed (Haas and Woerkom, 2016; Song and Choi, 2021). It resulted in more erosion. Accordingly, erosion can be categorized into two stages: the upstream and downstream phases of the erosion hole formation. The erosion intensity upstream of the erosion hole was significantly greater than downstream [Fig. 4(c)]. After the erosion hole occurred, subsequent *DFI* surges continued to scour away the erosion hole to increasing depths, while the bed soil downstream of the erosion hole experiences en-masse failure until erosion stops.

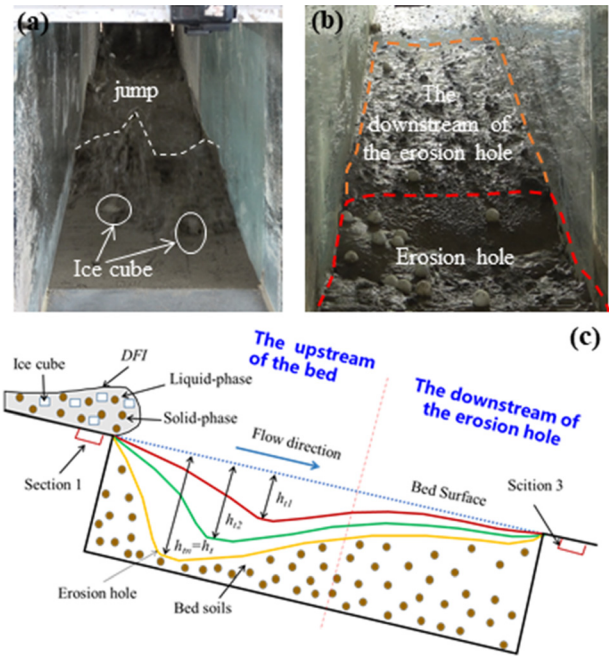

FIG. 4. The bed profile during the erosion process. (a) and (b) Profile of the bed before and after erosion. (c) Schematic diagram of the development of erosion. h_t is the eventual erosion depth. h_{t1}, h_{t2}, and h_{tn} represent the erosion depths during the time intervals t_1, t_2, and t_n, respectively.

Table II shows the measured results of the velocity and flow depth at different sections in the test. Figure 5 illustrates the

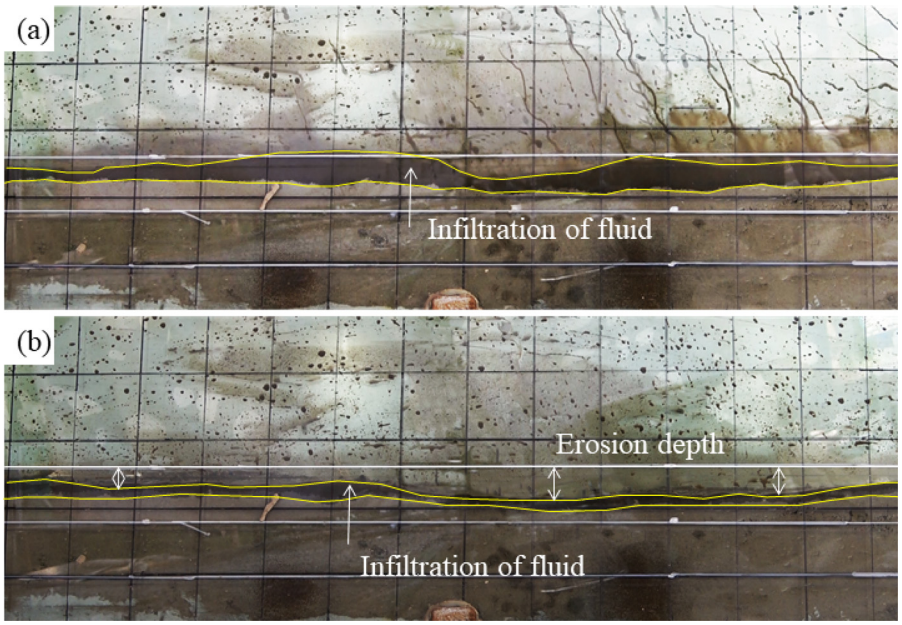

FIG. 3. Snapshots of *DFI* erosion process in the experiments. The white dotted lines indicate the top and bottom of the erodible bed. The area outlined in yellow is the extent of fluid infiltration. (a) Infiltration of fluid in the erosion process and (b) snapshot of bed side after the erosion process.

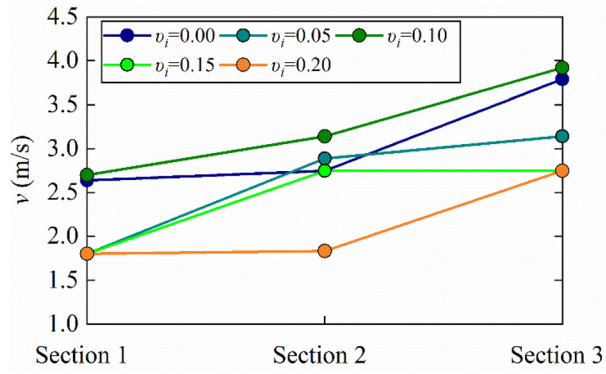

FIG. 5. The variation in the velocity with the monitored section. The water content of the bed soil is 8%.

changes in the velocity of the *DFI* with different ice contents in each section when the bed soil water content w is 8%. A significant increase in velocity occurs after the *DFI* passes through the top of the bed soil. The greatest rate of increase in the velocity of 74% occurs when v_i is 10%, whereas the rate of increase in the velocity is 44%–53% at the other ice contents. The rate of increase in the velocity increases with increasing ice content. This indicates that the *DFI* mobility increases after erosion, similar to the results of Pudasaini and Fischer (2020). This further demonstrates that the kinetic energy of the *DFI* after the erosion increases. This may be ascribed to the higher erosion volume in the erodible section. The growth rate of the *DFI* velocity after erosion was not significantly correlated with ice content. This is related to the interaction of the *DFI* and the bed soils. In general, the velocities of *DFI* after erosion are significantly greater than velocities before erosion, indicating that erosion promotes enhanced mobility.

Figure 6 illustrates the changes in flow depth when w is 8%. The peak flow depth occurs when the debris flow moves from the tank to the sensor position. The flow depth is 35 mm in the first section when the ice content is 5%. Then, the flow depth rapidly decreases to its lowest value in this section, which is essentially close to zero. The debris flow passes through the second section after a time interval of 0.158 s. The *DFI* is in contact with the bed soil. The flow depth decreases to 14.9 mm, after which it stops changing. The initial value of the flow depth at this section remains the same as the height of the non-erodible bed. This illustrates that deposition occurs after the *DFI* passes through the bed soils, and the deposition depth is the sum of the erosion depth and the residual flow depth. The time interval until the arrival of the *DFI* in the third section, which is 0.334 s, is longer than that in the second section (the interval distances were essentially the same). The *DFI* also takes more time to move through the third section, as deduced from the duration of the peak flow depth. However, Fig. 5 shows that the velocity is greatest in the third section. This illustrates that erosion increases the mobility of the *DFI*. At the different sections, the variations in flow depth with time show a similar trend, and the variations in the maximum flow depth with ice content are also similar. The duration of the peak flow depth at each section increases accordingly with increasing ice content, which corresponds to the variations in the velocity and erosion depth with increasing ice content.

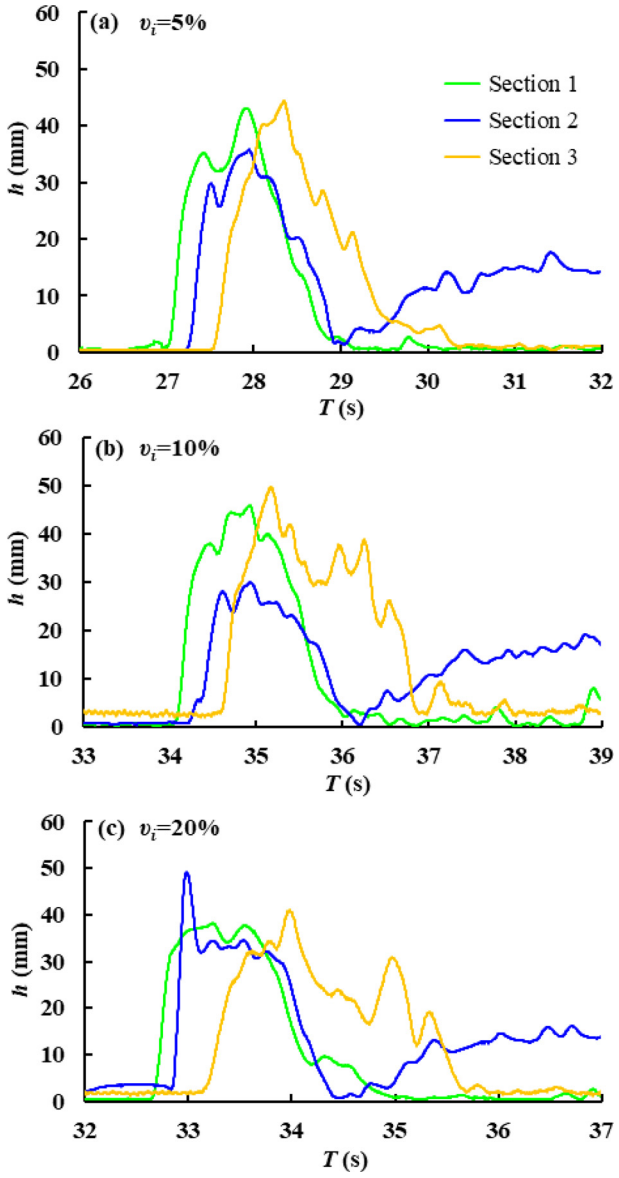

FIG. 6. The plot of the variation in flow depth with the monitoring section. (a)–(c) The ice contents are 5%, 10%, and 20%, respectively. The water content of the bed soil is 8%.

B. Distribution of erosion depth

Figure 7 shows that the erosion depth measured by the erosion columns varied with the water content in the bed soil. The distance from the interface between the non-erodible and erodible beds characterizes the distance of each erosion column along the flow direction from the non-erodible section upstream. For bed soils with different water contents, the peak erosion depth generally occurred at a distance of less than 0.3 m between the erodible section and non-erodible section. With increasing the water content of the bed soil, the maximum erosion depth ranged from 45–72, 27–54, and 30–60 mm, respectively.

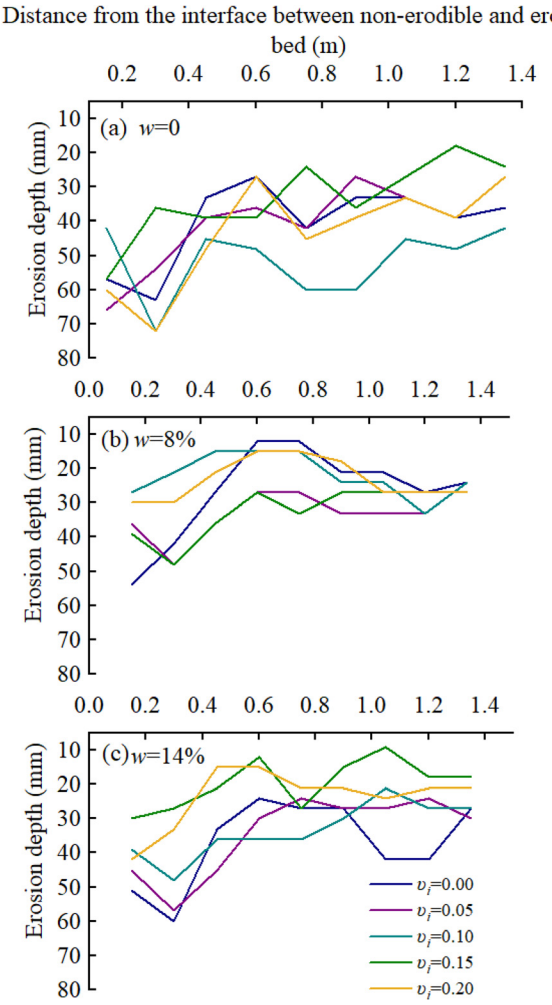

FIG. 7. Erosion profile measured by the erosion columns. (a)–(c) The water contents are 0%, 8%, and 14%, respectively.

Erosion holes form at the surface of the bed [Figs. 4(b) and 4(c)]. This is consistent with the previous studies (Haas and Woerkom, 2016; Song and Choi, 2021). Then, the erosion depth decreased gradually and reached a basically steady state in the midstream direction. The erosion depth changed within 15–25 mm. The erosion depth along the channel increased slowly in the downstream direction, and its fluctuation decreased. It may be attributed to the properties of the bed soil. In general, the erosion depth downstream of the erosion hole exhibited a fluctuating pattern. When bed soil water content increased, it ranged from 18–60, 12–36, and 9–45 mm, respectively. The flow velocity initially drops when the *DFIs* enter the erodible bed, after which a second surge increases flow velocity again further downstream (Haas and Woerkom, 2016). In addition, the erosion hole might deflect the *DFI* against gravity, leaving a reach with less erosion followed again by a reach of more erosion in the lower part of the erodible section, probably due to a bed-normal flow trajectory. This results in an inhomogeneous distribution of erosion depths. The erosion depth changes within 20–40 mm. The peak erosion depth is 72 mm when w is 0%. Then, the erosion depth fluctuated along the channel. However, the difference in the erosion depth is relatively small. When w is 8% and υ_i is 0%, the erosion depth is 54 mm at the first 0.15 m of the erodible bed. The minimum erosion depth of the bed soil is 12 mm for fluids with different ice contents, generally fluctuating around 30 mm. When the bed soil was saturated ($w = 14\%$) and no ice existed in the *DFI*, the maximum erosion depth occurred, and it changes relatively sharply along the channel. The erosion depth decreased with increasing proportion of ice in the debris flow at other ice contents, changing steadily along the channel. This phenomenon is extremely significant when the *DFI* moves to the midstream of the erodible bed. Figure 7 shows the linear relationship between the erosion depth and the water content of the bed soil was not significantly observed. The nearly saturated dry bed soils will be more easily eroded. This is consistent with the work of Song and Choi (2021). This can be attributed to the large difference between the strength of nearly saturated of dry bed soils and the shear stresses exerted by the *DFI* (Pudasaini and Fischer, 2020).

The spatial distribution of erosion depth is not uniform during the erosion process. Following the work of (Haas and Woerkom, 2016), the erosion asymmetry factor (A_{me}) was used to characterize the spatial erosion patterns of *DFI*. It characterizes the ratio between the maximum erosion depth in the upstream half of the erodible section and the maximum erosion depth in the downstream half of the section. It has been defined as follows:

$$A_{me} = \frac{\text{The maximum erosion depth}_{x=0-0.5L}}{\text{The maximum erosion depth}_{x=0.5L-L}}. \quad (2)$$

Figure 8 shows the variation of A_{me} with the ice content when the water content of the bed soil is different. A_{me} are all greater than 1. This confirms that erosion is greater upstream than downstream of the erodible bed, which is similar to the variation of erosion depth in Fig. 7. A_{me} exhibited a fluctuating pattern with the ice content increased. This may be ascribed to the variation of the peak erosion (Haas and Woerkom, 2016). Haas and Woerkom (2016) reported that A_{me} will increase with increasing the fraction of gravel and water content of *DFI*. In this study, as the ice content gradually increases from 0, the water content in the *DFI* gradually decreases, leading to a decrease in the peak erosion upstream of the erodible bed. A_{me} will also decrease based on Eq. (2). This trend will not last all the time. The gravel

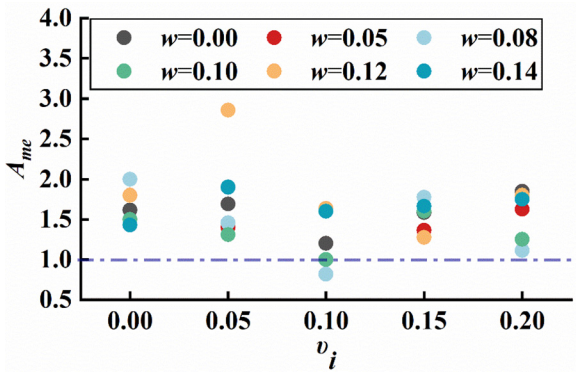

FIG. 8. The relationship between the erosion asymmetry factor and ice content.

fraction of the *DFI* increased as the ice content increased. The gravel fraction has a greater effect on erosion, resulting in another increase in the peak erosion upstream of the erodible bed and an increase in A_{me}. In addition, the fluctuating changes in erosion depth also induced a nonlinear variation of A_{me} with ice content. The relationship between A_{me} and bed soil water content was not observed significantly. After the *DFI* moved through the location of the peak erosion depth, a greater erosion depth will also occur downstream of the erodible bed. It will result in A_{me} not showing a significant correlation with the bed soil water content.

C. Pore pressure variation during erosion

Figure 9 shows the variation of pore pressure in bed soils at different bed soil water contents. In this study, the pore pressure sensor is located at the bottom of the erodible bed. When the fluid infiltrates into the bed soil, the water content of the bed soil will change, which causes the pore pressure of the bed soil to change. The pore pressure will be obtained using the sensor. The pore pressure is related to the erosion (Fig. 10). During the erosion process, the dry bed had the highest pore pressure, which was between 0.201 and 0.599 kPa. When the water content of the bed soil increased, the pore pressure gradually decreased. As the water content of the bed soil was greater than 10%, the pore pressure was stable, between 0.048 and 0.207 kPa. This indicated that the higher fluid infiltration in the dry bed, resulting in a higher pore pressure. This is because when the soil has a higher matric suction, its water absorption capacity is stronger (Chen *et al.*, 2024). As the water content of the bed soil increased, the large amount of water in the soil slowed down the rate of fluid infiltration in the bed soils, resulting in less pore pressure. The linear relationship between ice content and pore pressure was not significantly observed. It demonstrated that the infiltration of fluids was not affected by the ice.

During the erosion process, the pore pressure exhibited a parabola-like relationship with the bed water content [Fig. 10(a)]. The difference of the pore pressure was higher when *DFIs* with different ice contents eroded the dry bed. This may be the result of inhomogeneous infiltration of fluids in the bed soil. The difference of the pore pressure was less when *DFIs* with different ice contents eroded the other water

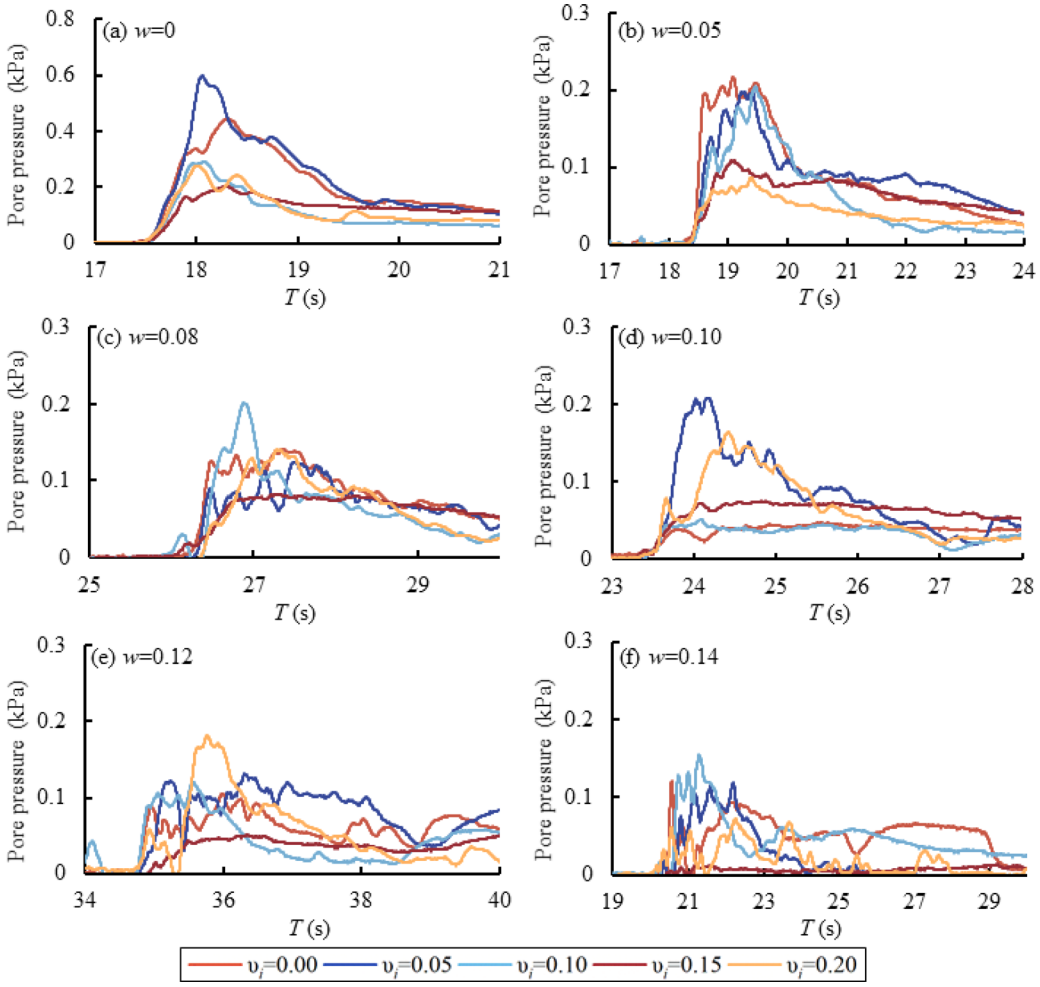

FIG. 9. Variation of pore pressure in bed soil when the water content of the bed soil increased. (a)–(c) The water content of the bed soil increased from 0% to 14%.

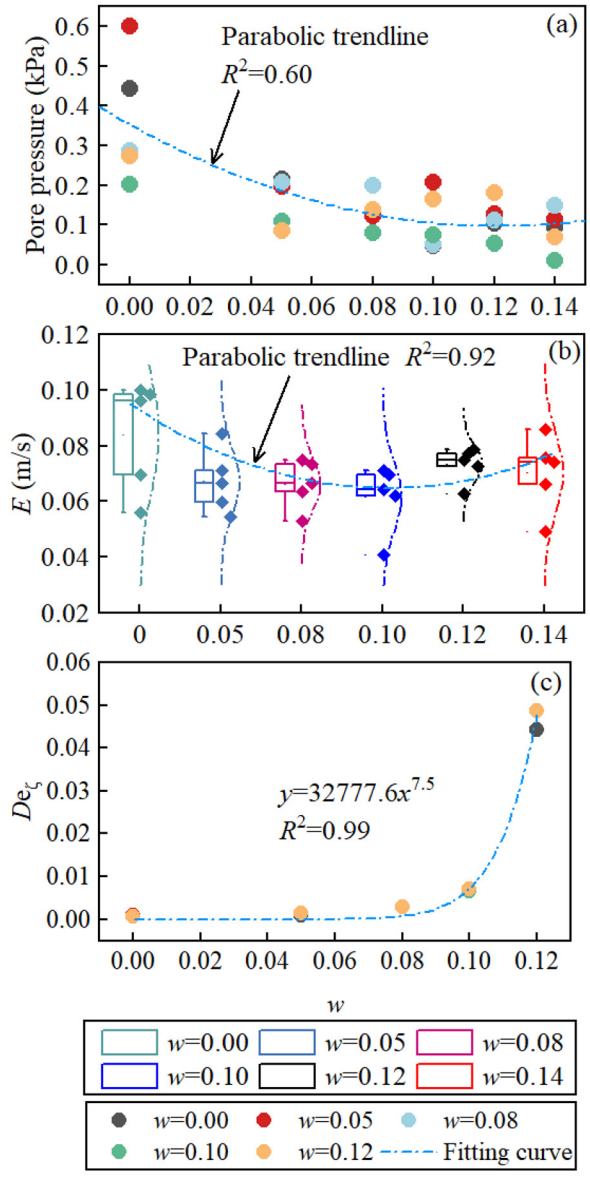

FIG. 10. Maximum pore pressure, erosion rate E, and Deborah number De_ζ with increasing the water content of the bed soil. (a) The fitting relationship between pore pressure and the water content of the bed soils is shown. (b) The relationship between the erosion rate and the bed water content. (c) The drained behavior of the bed soils.

content bed soil. This can be attributed to the fact that the water content of the bed soils was more homogeneous, and therefore, fluid infiltration was also more uniform compared to dry beds.

The erosion was related to the pore pressure of the bed soil (Iverson *et al.*, 2011; Zheng *et al.*, 2024). The relationship between the average erosion rate and bed soil water content is shown in Fig. 10(b). The average erosion rate is calculated by using the average depth divided by the erosion time. The erosion time is defined as the time it takes for the *DFI* to move through the entire erodible bed. A box plot was used to illustrate the relationship between the overall erosion rate and the water content [Fig. 10(b)]. The erosion rate exhibited a parabola-like relationship with the bed water content. This was similar to the relationship between the pore pressure and the bed water content. High pore pressure led to intense erosion. The erosion rate decreased with decreasing the pore pressure. After the bed water content is more than 10%, the pore pressure was gradually stable, while the erosion rate still increased. This is due to the inconsistent depth of erosion holes upstream on the erodible bed (Fig. 7). At the location of the erosion hole, the erosion is caused by the impact stress exerted by the *DFI* and is not dependent on the bed water content. High erosion depth upstream of the erodible bed resulted in an increase in the erosion rate, while the pore pressure was essentially unchanged.

During the erosion process, erosion is also affected by the shear behavior of the bed (Zheng *et al.*, 2024; Zheng *et al.*, 2023). To investigate this propensity, the Deborah number De_ζ was proposed by Zheng *et al.* (2023) to quantitatively evaluate. When the bed soil is saturated, De_ζ can be expressed by

$$De_\zeta = \frac{H^2}{Dt_e}. \tag{3}$$

When the bed soil is unsaturated, De_ζ can be expressed by

$$De_\zeta = \frac{K_i^2 t_e}{\Delta\theta^2 D}, \tag{4}$$

where H (m) is the erodible bed thickness; $D = k/(C\mu)$ is the pore pressure diffusion coefficient; k (m^2) is the bed permeability; C (m^2/N) is the drained compressibility of the bed soil; μ (Pa·s) is the fluid viscosity and can be calculated by the methods proposed by de Haas *et al.* (2015) and Roelofs *et al.* (2023): $\mu/\mu_w = 1 + 2.5\upsilon_{fines} + 10.05\upsilon_{fines}^2 + 0.002\,73^{16.6\upsilon_{fines}}$, where μ_w is the dynamic viscosity of pure water (0.001 002 Pa s) and υ_{fines} is the volume fraction of the interstitial fluid occupied by fines, which is calculated by the particle size distribution of the debris flow materials; t_e is the timescale during the erosion, which is defined as the time of movement of the *DFI* front through the whole bed; $K_i = k\rho_f g/\mu$ (m/s) is the hydraulic conductivity of saturated bed above the wetting front; and ρ_f is the density of the fluid phase of the *DFI*. Following the work of Chen *et al.* (2020). C and K_i were determined as 0.0013 and 2.97×10^{-5}m/s, respectively. θ_s and θ_i are the volumetric water content for saturated and initially unsaturated bed soil, respectively. $\Delta\theta$ is the water-content difference between these two beds. The volumetric water contents corresponding to the six bed sediment water contents (0, 5%, 8%, 10%, 12%, and 14%, respectively) in this study were 0, 0.06, 0.10, 0.13, 0.17, and 0.21, respectively. θ_s is 0.19 in this study.

Zheng *et al.* (2023) reported that the bed sediment overridden by debris flows can present drained behavior with $De_\zeta < 1$. In contrast, with $De_\zeta > 1$, it will lead to undrained behavior. Pore pressure dissipation is relatively limited, and the diffusion front originating along the shearing layer does not reach the boundaries. In this study, when the bed water content is 14%, the bed soil is saturated. De_ζ was more than 1000, leading to undrained behavior. This was because a permeable boundary was located at the bottom of the bed. Pore pressure dissipation is relatively limited (Zheng *et al.*, 2023). With the bed water content changing from 0% to 12%, the bed soil is unsaturated. The relationship between De_ζ and the bed water content is shown in

Fig. 10(c), indicating the exponential function relation. De_ζ increased dramatically after the bed water content was greater than 10%, while all were less than 1. This is ascribed to the sharp increase in the difference between the volumetric water content and the saturated water content of the bed soils. The bed sediment exhibited drainage behavior when it was unsaturated. This is because a permeable boundary located at the wetting front between an upper saturated zone and a lower unsaturated zone, where the water content is kept at the initial value (Zheng *et al.*,2023). Pore pressure dissipation is effective and can easily diffuse from the shearing bed to the boundaries within the erosion timescale.

D. Equation for erosion

The non-uniformity of the erosion depth is also related to the stresses exerted by debris flow. The collisional and shear stress are the two driving forces (Jiang *et al.*, 2023; Roelofs *et al.*, 2022). The collisional stress is less considered in the existing studies. In this study, the basal stresses were measured by the triaxial load cell. Table S1 shows the basal stresses measured at the location of section 1. The shear stress was basically between 0.050 and 0.119 kPa, and the normal stress was basically between 0.471 and 1.300 kPa. In the previous studies, the calculated erosion rate E is proportional to the difference between the shear stress exerted by the overlying flow τ and bed frictional stress τ_b (Iverson *et al.*, 2011; Zheng *et al.*, 2021), which is expressed by

$$E = \frac{\tau - \tau_b}{\rho v} = \frac{\tau - (\sigma - p)\tan\varphi}{\rho v}, \tag{5}$$

where σ is the normal stress of the *DFI*, p is the pore pressure of the bed soil, and φ is the bed soil friction angle.

Equation (5) is applied for saturated bed soils conditions. Song and Choi (2021) showed that the shear strength calculated for saturated conditions was still larger than the measured basal shear stress based on the data from Berger *et al.* (2011). Therefore, it showed that aside from friction-induced shear stresses, there should be other stresses (i.e., collisional stresses) contributing to the erosion of the soil bed. The collisional stress was evaluated as a driver of erosion in terms of mechanical mechanisms. However, the bed soils are unsaturated in nature. Equation (5) is not applied to be used for this conditions.

The text of Sec. III A showed that the infiltration in bed occurred during the erosion process. Although there was a parabola-like relationship between erosion rate and the bed water content, the differences were generally small. It can therefore be deduced that erosion was not dependent on the bed water content, while was related to the saturated layer on the bed surface during fluid infiltration. This is consistent with the work of Song *et al.* (2024). Therefore, the following equation can be used to calculate the shear strength for unsaturated conditions:

$$\tau_b = \Theta_c(\rho_s - \rho_f)g\delta, \tag{6}$$

where Θ_c is the critical Shields number and can be set to 0.15 following the work of Prancevic *et al.* (2014). δ can be denoted by D_{50}.

The model of erosion rate can be expressed by

$$E = \frac{\tau - \tau_b}{\rho v} = \frac{\tau - \Theta_c(\rho_s - \rho_f)gD}{\rho v}. \tag{7}$$

The collisional stress can be expressed by

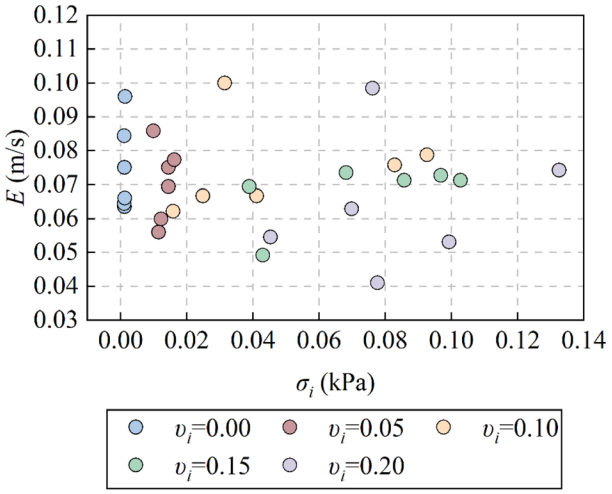

FIG. 11. The relationship between the erosion rate and collisional stress.

$$\sigma_i = \upsilon_s \rho_s \delta^2 \dot{\gamma}^2, \tag{8}$$

where υ_s is the solid volume fraction of the flow, ρ_s is the density of the flow particles, δ is characteristic grain size equal to D_{50}, and $\dot{\gamma}$ is the shear rate calculated by v/h.

Figure 11 shows the relationship between the erosion rate and the collisional stress. The solid volume fraction υ_s and characteristic particle diameter δ decreased with increasing the ice content, while the collisional stress increased. The fluid and bed conditions jointly control the erosion, leading to a non-significant linear relationship between erosion rate and collisional stress. We can conclude that Eq. (8) cannot be directly used to represent the contribution of the collisional stress to erosion.

To determine the contribution of the collisional stress to erosion, Eq. (7) can be transformed as the real stress τ^c inducing erosion. It can be expressed by

$$\tau^c = \tau_b + E\rho v. \tag{9}$$

The difference between τ^c and the measured τ can represent the contribution of the collisional stress to erosion.

Mesoscopic scaling was used in this study to ensure dynamic similarity between the front of a real debris flow and model flows. This type of scaling considers the grain-scale interactions, which ultimately gives rise to the macroscopic behavior of a debris flow (Iverson, 1997; Jiang *et al.*, 2023; and Song and Choi, 2021). The Savage number *Ns*, which characterizes the relative importance between collisional and frictional interparticle stresses, can be used for scaling the collisional flow fronts in this study,

$$N_s = \frac{\rho_s \delta^2 \dot{\gamma}^2}{(\rho_s - \rho_f)gh\tan\varphi'}, \tag{10}$$

where ρ_f is the fluid phase density and φ' is the effective friction angle of the solid grains in the flow.

Based on the measured data, the relationship between the dimensionless shear stress and Savage number *Ns* can be obtained, indicating a strong correlation between them (Fig. 12). With increasing ice

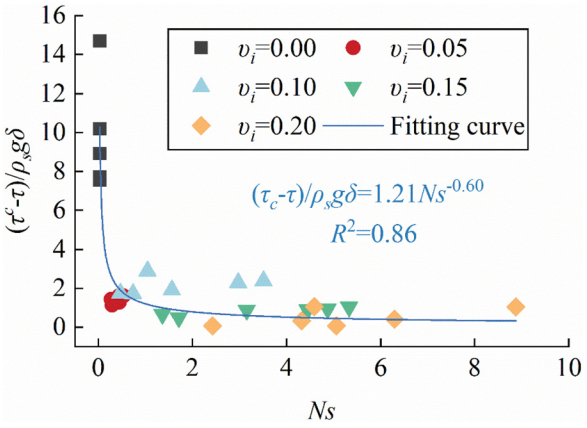

FIG. 12. Relationship between dimensionless shear stress and Savage number.

content, the gravel fraction increased, leading to an increasing in N_S. The flow regime of the *DFI* was collisional stress dominated. However, the increase in the ice content has also led to an increase in the characteristic grain size of the particles. $(\tau^c - \tau)/\rho_s g\delta$ decreased with increasing ice content. It can be expressed by

$$(\tau^c - \tau)/\rho_s g\delta = aN_s^b. \tag{11}$$

Both a and b are fitted constants.

Then, Eq. (9) can be transformed as

$$\tau^c = aN_s^b \rho_s g\delta + \tau. \tag{12}$$

Therefore, the erosion model considering the collisional stress can be expressed by

$$E = \frac{\tau^c - \tau_b}{\rho v} = \frac{(aNs^b \rho_s g\delta + \tau) - \Theta_c(\rho_s - \rho_f)gD}{\rho v}. \tag{13}$$

Equation (13) indicated that the contribution of the collisional stress to erosion can be expressed by

$$aN_s^b \rho_s g\delta = a\frac{\rho_s^{b+1}\delta^{2b+1}\dot{\gamma}^{2b}}{(\rho_s - \rho_f)^b g^{b-1} h^b (\tan\varphi')^b}, \tag{14}$$

when $b = -\frac{1}{2}$, $\tau^c - \tau = \frac{\rho_s^{\frac{1}{2}}\dot{\gamma}^{-1}}{(\rho_s-\rho_f)^{-\frac{1}{2}} g^{-\frac{3}{2}} (\tan\varphi')^{-\frac{1}{2}}}$, that is, $(\tau^c - \tau) \sim (\rho_s - \rho_f)gh\tan\varphi'$. When $b = 0$, $\tau^c - \tau = a\rho_s\delta g$, indicating that the erosion comes from the frictional stress and the collisional stress, that is, $(\tau^c - \tau) \sim \rho_s\delta$. Therefore, the contribution of the collisional stress to erosion is dependent on the value of b. When b was any other values, it indicated that erosion was affected by friction stresses and collision stresses together.

To evaluate the applicability of the model proposed in this study, a comparison of erosion rate calculated by Eq. (13) with the measured erosion rate was conducted. The results showed that the calculated values were in agreement with the measured erosion rates. A few deviations existed in some data. This may be attributed to the unstable flow regime during the erosion process.

In summary, the relationship between the erosion and the collisional stress was investigated in this study. The new erosion rate model was proposed by considering the effect of collisional stress. There were some errors in the calculated and measured erosion rates. The contribution term of collisional stress in the erosion model was treated as dimensionless. The relationship between the dimensionless contribution term of collisional stress and the flow parameters of the *DFI* was established. This approach is physically significant. Therefore, the model proposed by this study is applicable.

IV. DISCUSSION

The *DFI* is a unique type of glacial debris flow that contains ice. It is essential to investigate the effects of ice content in the fluid on the erosion. Considering the unsaturated characteristics of bed soil, the effect of its water content on erosion resistance needs to be studied. In this study, the erosion characteristics of *DFIs* along channels at different ice contents in the fluid and water contents in the bed soil were investigated.

A. Impact of ice on the erosion process

The impact of ice on the mobility of rock-ice avalanches has been reported. The mobility of rock-ice avalanches can be enhanced when ice is present. Ice is a low-friction material that can reduce friction within the propagating mass. The friction coefficient at the interface between the rock-ice mixture and the bed sediment decreases continuously with increasing ice content, and the distance that the flow moves increases accordingly (Yang *et al.*, 2019). The frictional heat induced at the sliding surface results in the melting of ice. The melting of ice further induces the fluidization of the fluid bed (Schneider *et al.*, 2011; Yang *et al.*, 2019). The density of the fluid decreases with increasing ice content, and the normal stress exerted on the bed decreases accordingly (Dong and Su, 2024). As the ice melts, the saturation of the bed soil increases, inducing lubrication of the sliding surface. The pore pressure increases accordingly. This consequently reduces the shear resistance of the bed sediment, resulting in the bed soil being easily entrained by the flowing material. It also contributes to facilitating the movement of rock-ice avalanches (Pudasaini and Krautblatter, 2014). The impact pressure increases with increasing ice content (Wang *et al.*, 2022a). This illustrates that the ability of the flow to produce a catastrophic event will be enhanced when ice exists. This is the reason why ice-rock avalanches in alpine mountains pose a significant threat.

The ice content in a *DFI* is generally less than that in rock-ice avalanches. The maximum ice content is defined as 20% in this study according to the work of Wang *et al.* (2023). The methods proposed by Wang *et al.* (2023) are used to calculate the energy produced by the phase transition below.

When the bed water content is 8%, the ice/water phase transition was quantified. The potential energy that can be supplied to the melting of ice comes from two sides: the gravitational potential energy of the fluid and the entrained material (i.e., P_r and P_e, respectively), which can be expressed by

$$P_r = -\varepsilon V(\upsilon_r\rho_r + \upsilon_i\rho_i + \upsilon_w\rho_w)g\Delta h, \tag{15}$$

$$P_e = -\varepsilon V'(\upsilon_r'\rho_r + \upsilon_w'\rho_w)g\Delta h', \tag{16}$$

where V (m^3) is the released volume, defined as 0.05. υ_r, υ_i, and υ_w are the rock, ice, and water fraction inside the released volume, respectively. ε is the fraction of gravitational potential energy of the initial landslide used on the heating and melting. ρ_r, ρ_i, and ρ_w are the

TABLE III. The energy used for ice melt; P_{relea} is the gravitational potential energy used for heating and melting, P_{entri} is the gravitational potential energy of the entrained material, and Q_L is the energy used for ice melt.

	A13	B13	C13	D13	E13
P_r (N m)	⋯	−1880.70	−1743.47	−1600.34	−1449.69
P_e (N m)	⋯	−725.55	−969.89	−597.11	−791.75
Q_L (J)	⋯	772 800	1 545 600	2 318 400	3 091 200

density of the rock, ice, and water in the *DFI*, respectively. Δh is the height difference between the mass center of the released volume and the alluvial fan. The value of Δh is 3.80 m, representing the height difference between top and tail of the flume. V' is the entrainment volume. υ_r' and υ_w' are the phase fraction of rock and water in the entrainment material. $\Delta h'$ is the height difference between the mass center of the entrainment material and the alluvial fan. The value of $\Delta h'$ is 1.90 m, representing the height difference of the erodible bed.

The energy used for ice melt Q_L is shown as follows:

$$Q_L = V\upsilon_i\rho_i L, \tag{17}$$

where $L = 3.36 \times 10^5$ J/kg is the latent heat of fusion of ice.

The results are shown in Table III. The sum of P_r and P_e was less than Q_L, indicating that the influence of phase transition on the dynamics of the *DFI* is minor. In the experiment of this study, the flume experiment was used to study the erosion characteristics of the *DFI* on a shorter spatial and temporal dimension, where the fluid lasted for only a few seconds and melting the ice by frictional heat generation alone is very challenging. In our experimental setup, the ice was treated as a low-friction solid material. This assumption was validated by the findings of Ren *et al.* (2021), Wang *et al.* (2022), and Yang *et al.* (2019), who reported that the average mass loss due to melting was less than 0.1% in each experiment. This indicates that significant melting of the ice did not occur, and the mixtures remained nearly dry after each experiment. Therefore, the effects of ice melting on erosion were deemed negligible in our study, and the ice was treated as a low-friction solid material in *DFI*.

When the ice is considered to be the solid material, the solid material concentration and the solid volume fraction are weighted averages of the volume fractions of the rock and ice (Dong and Su, 2024; Pudasaini and Krautblatter, 2014). The gravel fraction of the *DFI* will increase with increasing the ice content. This is equivalent to change the material composition of the *DFI*. The composition of debris flow can affect the erosion (Haas and Woerkom, 2016; Roelofs *et al.*, 2022). This is also a crucial factor contributing to the variability of *DFI* velocity, flow depth, and erosion depth during erosion (Figs. 5–7). In addition, the ratio of ice and water content in *DFI* has a significant effect on the erosion. The higher mobility can be obtained as the water content of the *DFI* is high (Wang *et al.*, 2023). When the water content increased, the flow discharge after the erosion will be enlarge. Table II shows that the velocity and the flow depth of the *DFI* were not influenced by the ice content. However, the flow discharge decreased with increasing the ice content. This is consistent with the work of Wang *et al.* (2023). It indicated that the influence of the water content in the *DFI* on its mobility was significant. The flow discharge after the erosion was more than it before the erosion, which showed that the erosion enhanced the mobility of the *DFI* (Pudasaini and Fischer, 2020). This is attributed to the interaction of the *DFI* with bed soil. When the total of the frictional stresses and collisional stresses was greater than the shear strength of the bed soil, erosion occurred. The particle velocity of the bed is not equal to zero until it is completely eroded. The kinetic energy of the fluid enhanced as the eroded bed materials entered into the fluid. In addition, the mass of the fluid increase induced an increase in its the kinetic energy. This was equivalent to the effectively reduced frictional stress (Pudasaini and Fischer, 2020). The mass production further enhanced the flow mobility, because the erosion-induced added mass implied added potential energy into the system.

The *DFIs* with a lower ice content have a higher mobility, while a closer flow discharge compared to other ice contents, which is related to entrainment of the bed sediment. This is also demonstrated that as the ice content increased, the more significant the contribution of erosion to the mobility of the *DFI*. Figures 5 and 6 show that a higher ice content of the *DFI* can significantly induce an increase in velocity or flow depth after the erosion, which resulted in an increase in the flow discharge (Fig. 13). We can be seen that the average flow rate increased

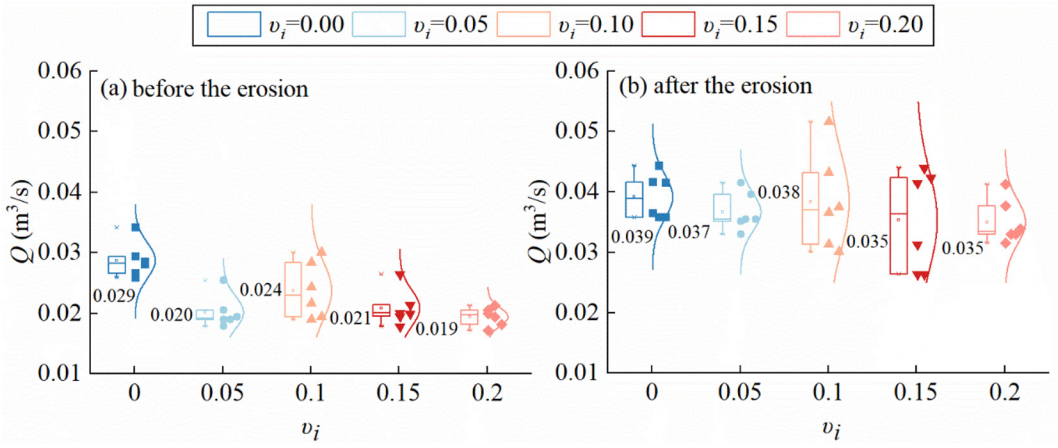

FIG. 13. The variation of the flow discharge Q with increasing ice content: (a) before the erosion and (b) after the erosion.

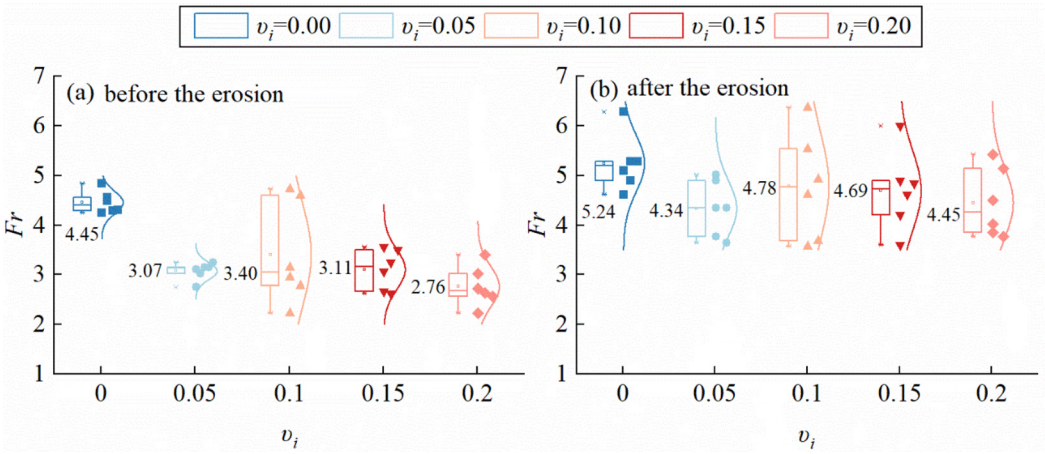

FIG. 14. The variation of *Fr* with increasing ice content: (a) before the erosion and (b) after the erosion.

from 0.019–0.029 m^3/s before erosion to 0.035–0.039 m^3/s after erosion, representing an increase of 34.48%–84.21%. The relationship between *Fr* and ice content before and after erosion was similar to the relationship between flow discharge and ice content. The average value of *Fr* ranged from 2.76–4.45 before erosion, while it ranged from 4.34–5.24 after erosion. The specific data are shown in Table II. The data in section 1 and section 3 represented the values before and after erosion, respectively. The *DFIs* with a lower ice content have a higher *Fr*, indicating a higher mobility as well (Fig. 14). As the ice content increased, *Fr* changed less after erosion. This demonstrated that the mobility of the *DFI* was controlled by the entrainment.

B. Effect of bed sediment wetness on the erosion

The bed conditions are the important factor influencing the erosion. The pore pressure will be changed when debris flow moved the erodible bed. The pore pressure correlated with the bed water content. Erosion of the *DFI* was accompanied by the process of fluid infiltration in the erodible bed (Fig. 3). Therefore, the pore pressure of the bed soil is dependent on its permeability characteristics.

Figure 10(a) shows that peak pore pressures were significantly greater in the bed soils with low water content than with the high water content during erosion. This demonstrated that the infiltration rate was greater in the bed soils with low water content during the *DFI* moved through the erodible bed, which resulted in a significant change in the pore pressure. This is also dependent on the water retention capacities of the bed soils. Table I shows that the bed soils with low water content have the higher matric suction, and then, they are more absorbent and the fluid can be easily infiltrated. However, this is not consistent with the work of Iverson *et al.* (2011) and Zheng *et al.* (2024). There may be two reasons for this: First, the composition of the bed soils was different. In this study, the composition of the bed soil and two-phase mixtures remained consistent. In the previous studies, the grain size of the bed soils is mostly homogeneous or lacks fine-grained material, resulting in different water retention capacities. Zheng *et al.* (2021) showed that the pore pressure of the bed soils with the higher water content was less when debris flow eroded the widely graded bed sediment. Second, it may be attributed to the differences caused by the location of measurements of the pore pressure in this study. In the different location of the erodible bed, the erosion depth was different (Fig. 8). It indicated that the infiltration phenomenon of the bed soils at different locations was also not uniform, resulting in differences in the pore pressure. This can be proved by the work of Iverson *et al.* (2011), who have reported that pore pressure measured downstream of the erodible bed was greater than upstream.

The erosion influenced by the pore pressure of the bed soils. Figures 10(a) and 10(b) show that the relationship between the pore pressure and the bed water content was similar to the relationship between the erosion rate and the bed water content. The high pore pressure can reduce basal friction between particles and contribute to entrainment (Iverson *et al.*, 2011; Li *et al.*, 2024; and Roelofs *et al.*, 2022). The higher pore pressure led to a reduction in the shear strengthen of the bed soil. The difference between the stresses exerted by the *DFI* and the shear strengthen decreased. Therefore, the higher erosion rate occurred when the bed soil was nearly dry or saturated. The pore pressure was influenced by the drainage behavior of the bed sediment overridden by debris flows (Zheng *et al.*, 2024; Zheng *et al.*, 2023). The Deborah number De_ζ proposed by Zheng *et al.* (2024) was used to evaluate this propensity [Fig. 10(c)]. The unsaturated bed soils all represented the drained behavior. It demonstrated that the bed soils were easy to be eroded as shear contraction occurred. In contrast, the saturated bed soils represented the undrained behavior. It demonstrated that the bed soils were difficult to be eroded as shear dilation occurred. Theoretically, pore water pressure was lower when the bed sediment exhibited a drained behavior, in contrast to an undrained behavior (Zheng *et al.*, 2024). This is not consistent with the result of this study. This was attributed to the fact that pore pressure was influenced by the saturated layer at the bed surface (Roelofs *et al.*, 2023; Zheng *et al.*, 2023). The bed soil has the high permeability under unsaturated conditions. The bed boundaries were easy to drain. However, the penetration depth of the fluid in the bed soil will increase. This undoubtedly increased the difficulty of drainage and led to a rise in pore pressure. Under the saturated conditions, the bed soil has the low permeability. The bed boundaries were difficult to drain. The pore pressure will also increase.

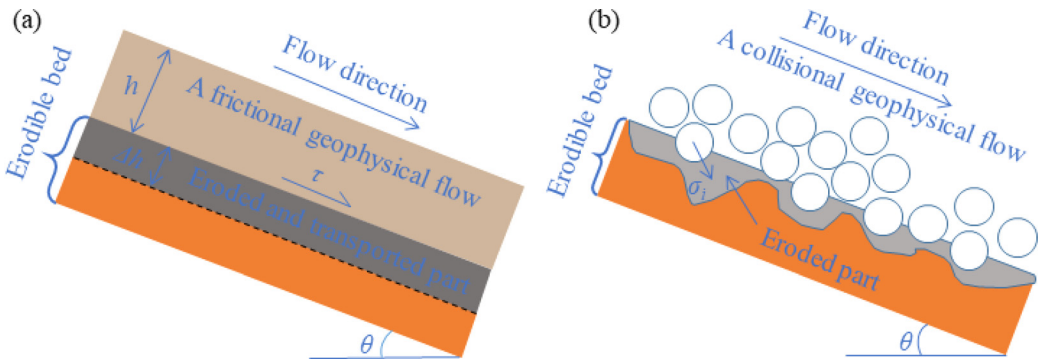

FIG. 15. Schematic illustration of two mechanisms of erosion: (a) friction-induced erosion stress τ and (b) collision-induced erosion stress σ_i. (Jiang *et al.* 2023).

C. The applicability of erosion equation

The collisional stress is the important force to drive the erosion. Unlike friction-induced erosion, collision-induced erosion is caused by instantaneous and discrete impacts on a soil bed (Song and Choi, 2021). The ice content of the *DFI* induced the increase in the gravel fractions, which resulted in an increase in the collisional stress. The previous studies have shown that erosion induced by collisional stresses led to the formation of irregular protrusions on the bed surface, making it uneven (Fig. 15) (Jiang *et al.*, 2023). This also caused the erosion depth to exhibit fluctuating changes. This is consistent with the result of this study. McArdell *et al.* (2007) demonstrated that coarse particles at a debris flow front do not exhibit enduring contact with each other. Therefore, the effects of frictional stress are limited. This further illustrates the important contribution of collisional stress to erosion. The segregation phenomenon will occur during movement of the *DFI* (Zhou *et al.*, 2024; Zhu *et al.*, 2024). In addition, the ice density is less than the density of solid particles and fluid. The solid material comprising the ice and rock will also not exhibit enduring contact with each other. Therefore, collisional stresses are also the driving force behind *DFI* erosion.

The shear stresses exerted by debris flows in the existing erosion rate models dominated by frictional stresses and collisional stresses are not considered. The model based on the contribution of collisional stresses was proposed by this study [Eq. (13)]. This is applicable to the erosion process of the *DFI*. The collisional stress and frictional stress induced the erosion together. Therefore, the two erosion mechanisms shown in Fig. 15 all existed in the erosion process of the *DFI*. The model in this study is related to the Savage number *Ns*. It demonstrates that Eq. (13) is of physical significance. This indicated that erosion is related to the physical state of the fluid. Physical erosion mechanisms of *DFI* were elucidated.

A comparison was conducted between the proposed model and those proposed by Pudasaini and Fischer (2020) and Choi and Song (2023); the results are shown in Fig. 16. For the calculations of these models, see Text S1 and Table S2. The model proposed by Pudasaini and Fischer (2020) is a two-phase model, which comprises two aspects: the solid erosion rate E_s and the fluid erosion rate E_f.

The results showed that the erosion rate calculated by the model in this study was basically close to that calculated by the two-phase model [Fig. 16(a)]. The contribution of collisional stress was

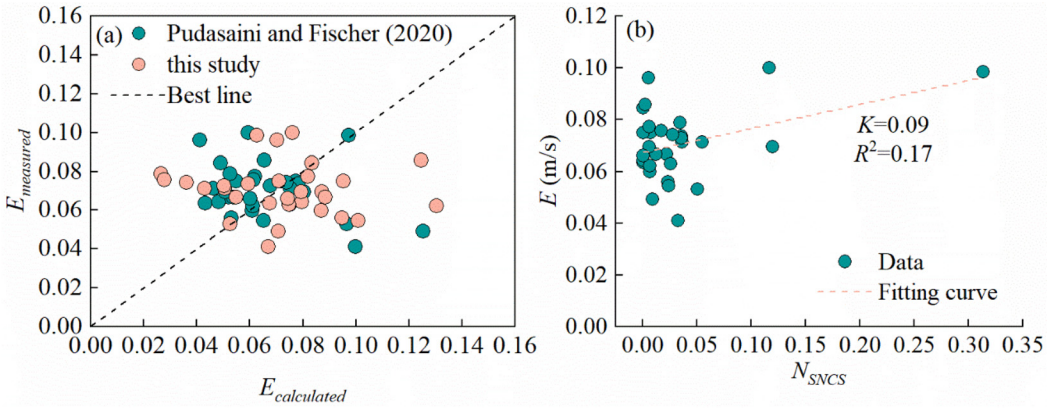

FIG. 16. Comparison between the proposed model and those proposed by Pudasaini and Fischer (2020) and Choi and Song (2023): (a) comparison between the measured erosion rate and the erosion rate calculated by the proposed model and Pudasaini and Fischer (2020) and (b) the relationship between the erosion rate and the strength normalized collisional stress.

considered in the model proposed by this study. Therefore, the model in this study was significantly applicable. However, the model proposed by Song and Choi (2021) and Choi and Song (2023) was not reliable to the erosion of the *DFI* [Fig. 16(b)]. The correlation between erosion rate and the strength normalized collisional stress N_{SNCS} was low (R^2=0.17). This is because the physical significance of the proportional coefficients K in the model was not clear.

The equation of the unsaturated shear strength used in this study can reflect the infiltration phenomenon during the erosion process. This is consistent with the research of Song *et al.* (2024). Although some errors existed when the model is used to calculate the erosion rate of the *DFI*, it is still applicable.

D. Uncertainty analysis

The effects of ice content and bed wetness on erosion of *DFI* were analyzed in this study. The erosion model considering the contribution of the collisional stress was proposed. This contributed to the understanding of the *DFI* dynamics. However, the applicability of the results to natural events in the field needs to be further investigated.

The similarity between the experiment and the real event is crucial (Iverson, 2015). The Froude number *Fr* was used to determine the effect of the scale discrepancy between laboratory debris flows and natural events. The value of *Fr* ranged from 2.2 to 6.4. It is within the range to be controlled by the experiment. Therefore, the experimental results in this paper are reliable. Miniaturized debris flows exhibit disproportionately large effects of viscous shear resistance and cohesion as well as disproportionately small effects of excess pore pressure that is generated by debris dilation or contraction. This may induce the difference between the experimental results and natural events in the field (Iverson, 2015).

In addition, the applicability of the proposed model needs to be further evaluated. Figure 17 indicates that the calculated erosion rate was close to the measured erosion rate. To further validate the applicability of the model, the three dimensionless numbers were used (the mean average of the relative error *MARE*, the Theil inequality coefficient *TIC*, and the prediction accuracy factor *PAF*) (Wang *et al.*, 2018). The *MARE* and *TIC* indices ranges from 0 to 1, and lower values of them denote better performance of the model. A *PAF* value of 1.00 indicates the predicted values are closer to the measured value. The values of *MARE*, *TIC*, and *PAF* for the proposed model are 0.33, 0.06, and 1.35, respectively. Therefore, the proposed model is applicable. The solid volume fraction of the *DFI* was lower in this study. Whether the model can be applied to a higher solid volume fraction of the *DFI* requires further evaluation with additional data samples. In addition, numerical simulation methods are also an effective method to validate the applicability of a model. Due to the lack of information on natural events in the field, the values of the dynamic parameters of *DFIs* need to be obtained in the future based on field investigation, monitoring and numerical simulation methods to further validate the reliability of the proposed model.

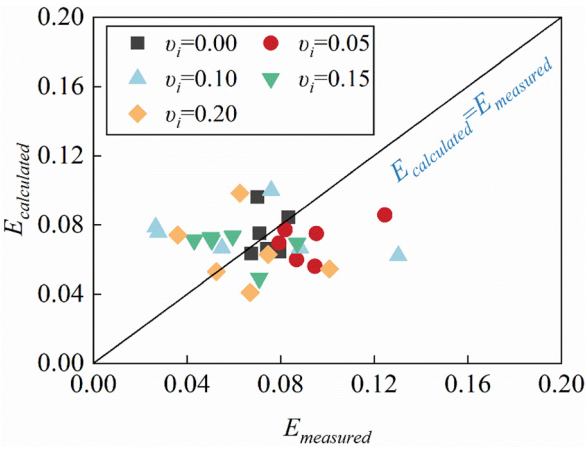

FIG. 17. Comparison between the calculated erosion rate $E_{calculated}$ and measured erosion rate $E_{measured}$.

The experiments in this study were conducted on a shorter spatial and temporal dimension, and the phase transition was not considered. However, there are complex heat exchange phenomena during the long-distance movement of the *DFIs* (Pudasaini and Krautblatter, 2014; Pudasaini, 2024; and Schneider *et al.*, 2011). Heat generation due to shear between the fluid and the bed soils will lead to melting of the ice, thus changing the flow regime of the fluids. The new experimental instruments that can observe the movement of ice and the resulting melting phenomena are need to be designed in the future.

V. CONCLUSIONS

The effect of fluid ice content and bed wetness on the erosion of the *DFI* was investigated in this study, and the following conclusions were drawn:

(1) The spatial distribution of the erosion depth is asymmetrical during the erosion. Maximum erosion depth occurred within 0.3 m upstream of the erodible bed, up to 72 mm. The erosion depth downstream of the bed fluctuated, basically ranged from 3 to 60 mm. A_{me} increases and then decreases with increasing the ice content. The erosion pattern of en-masse failure was observed in this study. Erosion and fluid infiltration occurred simultaneously during the erosion process. The erosion rate exhibits parabola-like relationship with the bed water content.

(2) The linear relationship between the velocity or the flow depth before and after the erosion and the ice content is not observed significantly. The velocity after the erosion is enhanced, and the growth rate ranged from 10.6% to 103.3%. The mobility of the *DFI* is not affected by the ice content, while is related to the ice/water ratio in the *DFI*.

(3) The pore pressure of the bed soils shows a decreasing trend with water content, which is basically consistent with the relationship between erosion rate and water content. It demonstrated that the erosion is influenced by the pore pressure. The bed sediment overridden by the *DFI* all represents drained behavior under unsaturated conditions. This propensity indicates that shear contraction of the bed soil occurs during erosion and that the soil is easily eroded. While the bed soil is saturated, it represents undrained behavior, indicating that shear dilation of the bed soil occurs. The bed soils are difficult to be eroded.

(4) The erosion rate model proposed is based on the contribution of the collisional stress. A comparison erosion rate calculated by the model in this study with the measured erosion rate showed that the two are in agreement. This indicates that the model in this study is applicable.

SUPPLEMENTARY MATERIAL

See the supplementary material for the following: Table S1 showing the data of the basal stresses measured at section 1 in this study, which can be available through the journal's designated website; Table S2 indicating that a comparison between the proposed model and the model proposed by Pudasaini and Fischer (2020) and Choi and Song (2023) was conducted; and the erosion model proposed by Pudasaini and Fischer (2020) and Choi and Song (2023) in Text.S1.

ACKNOWLEDGMENTS

This study was supported by the Second Tibetan Plateau Scientific Expedition and Research Program (Grant No. 2019QZKK0904), the Nyingchi National Sustainable Development Experimental Zone Project (2023-SYQ-007), the Science and Technology Research Program of Institute of Mountain Hazards and Environment, Chinese Academy of Sciences (Grant No. IMHE-ZDRW-02), and the Chinese Academy of Sciences Light of West China Program.

AUTHOR DECLARATIONS

Conflict of Interest

The authors have no conflicts to disclose.

Author Contributions

Xiangning Li: Conceptualization (equal); Data curation (equal); Formal analysis (equal); Investigation (equal); Methodology (equal); Writing – original draft (equal). **Jiangang Chen:** Funding acquisition (equal); Investigation (equal); Supervision (equal); Writing – review & editing (supporting). **Xiaoqing Chen:** Funding acquisition (equal); Investigation (supporting); Writing – review & editing (supporting). **Xi'an Wang:** Investigation (supporting); Writing – review & editing (supporting). **Jinshui Wang:** Investigation (supporting); Writing – review & editing (supporting). **Hechun Ruan:** Investigation (supporting); Writing – review & editing (supporting). **Min Huang:** Investigation (supporting); Writing – review & editing (supporting).

DATA AVAILABILITY

The data that support the findings of this study are available within the article and its supplementary material.

REFERENCES

Allen, S. K., Rastner, P., Arora, M., Huggel, C., and Stoffel, M., "Lake outburst and debris flow disaster at Kedarnath, June 2013: Hydrometeorological triggering and topographic predisposition," Landslides **13**, 1479–1491 (2016).

Berger, C., McArdell, B. W., and Schlunegger, F., "Direct measurement of channel erosion by debris flows, Illgraben, Switzerland," J. Geophys. Res. **116**, F01002, https://doi.org/10.1029/2010JF001722 (2011).

Breien, H., De Blasio, F. V., Elverhøi, A., and Høeg, K., "Erosion and morphology of a debris flow caused by a glacial lake outburst flood, Western Norway," Landslides **5**, 271–280 (2008).

Chen, H., Du, H., Guo, H. T. *et al.*, "Freezing strain characteristics and mechanisms of unsaturated frozen soil: Analysis of matric suction and water–ice phase change," Acta Geotech. **19**, 7243–7260 (2024).

Chen, H. X. and Zhang, L. M., "EDDA 1.0: Integrated simulation of debris flow erosion, deposition and property changes," Geosci. Model Dev. **8**, 829–844 (2015).

Chen, L. L., Zhou, G. G. D., Mu, Q. Y., Cui, K. F. E., and Song, D. R., "Compression characteristics of saturated re-compacted glacial tills in Tianmo Gully of Tibet, China," J. Mountain Sci. **16**, 1661–1674 (2020).

Chiarle, M., Iannotti, S., Mortara, G., and Deline, P., "Recent debris flow occurrences associated with glaciers in the Alps," Global Planet. Change **56**, 123–136 (2007).

Choi, C. E., Au-Yeung, S. C. H., Ng, C. W. W., and Song, D. "Flume investigation of landslide granular debris and water runup mechanisms," Géotech. Lett. **5**, 28–32 (2015).

Choi, C. E. and Song, P., "New unsaturated erosion model for landslide: Effects of flow particle size and debunking the importance of frictional stress," Eng. Geol. **315**, 107024 (2023).

Cui, P., Zeng, C., and Lei, Y., "Experimental analysis on the impact force of viscous debris flow," Earth Surf. Processes Landforms **40**, 1644–1655 (2015).

de Haas, T., Braat, L., Leuven, J. R. F. W., Lokhorst, I. R., and Kleinhans, M. G., "Effects of debris flow composition on runout, depositional mechanisms, and deposit morphology in laboratory experiments," J. Geophys. Res. **120**, 1949–1972, https://doi.org/10.1002/2015JF003525 (2015).

Dong, Z. B. and Su, L. J., "Flow regimes and basal normal stresses in rock–ice avalanches by experimental rotating drum tests," Cold Reg. Sci. Technol. **218**, 104081 (2024).

Evans, S. G., Bishop, N. F., Fidel Smoll, L., Valderrama Murillo, P., Delaney, K. B., and Oliver-Smith, A., "A re-examination of the mechanism and human impact of catastrophic mass flows originating on Nevado Huascarán, Cordillera Blanca, Peru in 1962 and 1970," Eng. Geol. **108**, 96–118 (2009).

Gao, B., Zhang, J. J., Wang, J. C., Chen, L., and Yang, D. X., "Formation mechanism and disaster characteristics of debris flow in the Tianmo gully in Tibet," Hydrogeol. Eng. Geol. **46**(05), 144–153 (2019) (in Chinese).

Ge, Y. G., Cui, P., Su, F. H., Zhang, J. Q., and Chen, X. Z., "Case history of the disastrous debris flows of Tianmo Watershed in Bomi County, Tibet, China: Some mitigation suggestions," J. Mt. Sci. **11**, 1253–1265 (2014).

Guo, R., Jiang, L., Xu, Z., Li, C., Huang, R., Zhou, Z., Li, T., Liu, Y., Wang, H., and Fan, X., "Seismic and hydrological triggers for a complex cascading geohazard of the Tianmo Gully in the southeastern Tibetan Plateau," Eng. Geol. **324**, 107269 (2023).

Han, Z., Chen, G., Li, Y., and He, Y., "Assessing entrainment of bed material in a debris-flow event: A theoretical approach incorporating Monte Carlo method," Earth Surf. Processes Landforms **40**, 1877–1890 (2015).

Han, Z., Wang, W., Li, Y., Huang, J., Su, B., Tang, C., Chen, G., and Qu, X., "An integrated method for rapid estimation of the valley incision by debris flows," Eng. Geol. **232**, 34–45 (2018).

Haas, T. D. and Woerkom, T. V., "Bed scour by debris flows: experimental investigation of effects of debris-flow composition," Earth Surface Processes Landforms **41**, 1951–1966 (2016).

Iverson, R. M., "The physics of debris flows," Rev. Geophys. **35**, 245–296, https://doi.org/10.1029/97RG00426 (1997).

Iverson, R. M., Reid, M. E., Logan, M., LaHusen, R. G., Godt, J. W., and Griswold, J. P., "Positive feedback and momentum growth during debris-flow entrainment of wet bed sediment," Nat. Geosci. **4**, 116–121 (2011).

Iverson, R. M., "Scaling and design of landslide and debris-flow experiments," Geomorphology **244**, 9–20 (2015).

Jiang, Y., Song, P., Choi, C. E., and Choo, J., "Erosion and transport of dry soil bed by collisional granular flow: Insights from a combined experimental-numerical investigation," J. Geophys. Res. **128**, e2023JF007073, https://doi.org/10.1029/2023JF007073 (2023).

Li, P., Wang, J. D., Hu, K. H., Qiu, H. J., and Xie, J. L., "Experimental investigation on debris flow resistance and entrainment characteristics: Effects of the erodible bed with discontinuous grading," J. Mt. Sci. **19**, 2397–2419 (2022).

Li, P., Wang, J., Hu, K., and Shen, F., "Effects of bed longitudinal inflexion and sediment porosity on basal entrainment mechanism: Insights from laboratory debris flows," Landslides **18**, 3041–3062 (2021).

Li, P., Wang, J., Hu, K., and Xie, J., "Shedding effects of sediment composition and bed morphology on debris flow dynamics and entrainment mechanism: Insights from laboratory experiments," Eng. Geol. **333**, 107495 (2024).

McArdell, B. W., Bartelt, P., and Kowalski, J., "Field observations of basal forces and fluid pore pressure in a debris flow," Geophys. Res. Lett. **34**(7), L07406, https://doi.org/10.1029/2006GL029183 (2007).

McCoy, S. W., Kean, J. W., Coe, J. A., Tucker, G. E., Staley, D. M., and Wasklewicz, T. A., "Sediment entrainment by debris flows: In situ measurements from the headwaters of a steep catchment," J. Geophys. Res. **117**, F03016, https://doi.org/10.1029/2011JF002278 (2012).
McDougall, S. and Hungr, O., "Dynamic modelling of entrainment in rapid landslides," Can. Geotech. J. **42**, 1437–1448 (2005).
Ng, C. W. W., Zheng, M., Liu, H., and Poudyal, S., "Effects of bed hydrophobicity on post-fire debris flow entrainment and momentum growth," J. Geophys. Res. **127**, e2022JF006783, https://doi.org/10.1029/2022JF006783 (2022).
Peng, D., Zhang, L., Jiang, R., Zhang, S., Shen, P., Lu, W., and He, X., "Initiation mechanisms and dynamics of a debris flow originated from debris-ice mixture slope failure in southeast Tibet, China," Eng. Geol. **307**, 106783 (2022).
Prancevic, J. P., Lamb, M. P., and Fuller, B. M., "Incipient sediment motion across the river to debris-flow transition," Geology **42**, 191–194 (2014).
Pudasaini, S. P., "A general two-phase debris flow model," J. Geophys. Res. **117**, F03010, https://doi.org/10.1029/2011JF002186 (2012).
Pudasaini, S. P., "A multi-phase thermo-mechanical model for rock-ice avalanche," arXiv:2404.06130 (2024).
Pudasaini, S. P. and Fischer, J. T., "A mechanical erosion model for two-phase mass flows," Int. J. Multiphase Flow **132**, 103416 (2020).
Pudasaini, S. P. and Krautblatter, M., "A two-phase mechanical model for rock-ice avalanches," J. Geophys. Res. **119**, 2272–2290, https://doi.org/10.1002/2014JF003183 (2014).
Pudasaini, S. P. and Mergili, M., "A multi-phase mass flow model," J. Geophys. Res.**124**, 2920–2942, https://doi.org/10.1029/2019JF005204 (2019).
Ren, Y., Yang, Q., Cheng, Q., Cai, F., and Su, Z., "Solid-liquid interaction caused by minor wetting in gravel-ice mixtures: A key factor for the mobility of rock-ice avalanches," Eng. Geol. **286**, 106072 (2021).
Roelofs, L., Colucci, P., and de Haas, T., "How debris-flow composition affects bed erosion quantity and mechanisms: An experimental assessment," Earth Surf. Processes Landforms **47**, 2151–2169 (2022).
Roelofs, L., Nota, E. W., Flipsen, T. C. W., Colucci, P., and de Haas, T., "How bed composition affects erosion by debris flows—An experimental assessment," Geophys. Res. Lett. **50**, e2023GL103294, https://doi.org/10.1029/2023GL103294 (2023).
Schneider, D., Kaitna, R., Dietrich, W. E., Hsu, L., Huggel, C., and McArdell, B. W., "Frictional behavior of granular gravel–ice mixtures in vertically rotating drum experiments and implications for rock–ice avalanches," Cold Reg. Sci. Technol. **69**, 70–90 (2011).
Shieh, C. L., Jan, C. D., and Tsai, Y. F., "A numerical simulation of debris flow and its application," Nat. Hazards **13**(1), 39–54 (1996).
Song, D., Chen, X., Zhou, G. G. D., Lu, X., Cheng, G., and Chen, Q., "Impact dynamics of debris flow against rigid obstacle in laboratory experiments," Eng. Geol. **291**, 106211 (2021).
Song, P. and Choi, C. E., "Revealing the importance of capillary and collisional stresses on soil bed erosion induced by debris flows," J. Geophys. Res. **126**, e2020JF005930, https://doi.org/10.1029/2020JF005930 (2021).
Song, P., Yang, J., Choi, C. E., and Zhang, J., "Experimental Investigation on scouring v.s. mass failure of unsaturated soil bed: Implications for debris flow initiation and erosion," J. Geophys. Res. **129**, e2023JF007275, https://doi.org/10.1029/2023JF007275 (2024).
Wang, C., Cui, Y., Song, D., Nie, J., and Hu, B., "Effect of ice content on the interaction between rock–ice avalanche and rigid barrier: Physical and numerical modelling," Comput. Geotech. **150**, 104924 (2022a).
Wang, T., Chen, J., Chen, X., You, Y., and Cheng, N., "Application of incomplete similarity theory to the estimation of the mean velocity of debris flows," Landslides **15**, 2083–2091 (2018).
Wang, T., Huang, T., Shen, P., Peng, D., and Zhang, L., "The mechanisms of high mobility of a glacial debris flow using the Pudasaini-Mergili multi-phase modeling," Eng. Geol. **322**, 107186 (2023).
Wang, Z., Ma, C., Hu, K., Liu, S., and Lyu, L., "Investigation of initiation conditions of periglacial debris flows in Sanggu watershed, Eastern Himalayas, Tibet Plateau (China)," Landslides **20**, 813–827 (2022b).
Wang, Z., Hu, K. H., Ma, C., Li, Y., and Liu, S., "Landscape change in response to multiperiod glacial debris flows in Peilong catchment, southeastern Tibet," J. Mt. Sci. **18**, 567–582 (2021).
Wei, R. Q., Zeng, Q. L., Davies, T., Yuan, G. X., Wang, K. Y., Xue, X. Y., and Yin, Q. F., "Geohazard cascade and mechanism of large debris flows in Tianmo gully, SE Tibetan Plateau and implications to hazard monitoring," Eng. Geol. **233**, 172–182 (2018).
Whipple, K. X. and Tucker, G. E., "Dynamics of the stream-power river incision model: Implications for height limits of mountain ranges, landscape response timescales, and research needs," J. Geophys. Res. **104**(B8), 17661–17674, https://doi.org/10.1029/1999JB900120 (1999).
Yang, Q., Su, Z., Cheng, Q., Ren, Y., and Cai, F., "High mobility of rock-ice avalanches: Insights from small flume tests of gravel-ice mixtures," Eng. Geol. **260**, 105260 (2019).
Zheng, H. C., Shi, Z. M., Yu, S. B., Fan, X. M., Hanley, K. J., and Feng, S. J., "Erosion mechanisms of debris flow on the sediment bed," Water Resour. Res. **57**, e2021WR030707, https://doi.org/10.1029/2021WR030707 (2021).
Zheng, H. C., Shi, Z. M., Hanley, K. J., Zhou, Y. Y., and Hu, X. L., "Pore pressure evolution in bed sediment overridden by debris flow: A general formulation," Earth Surf. Processes Landforms **48**, 1188–1201 (2023).
Zheng, H. C., Hu, X. L., Shi, Z. M., Shen, D. Y., and De Haas, T., "Deciphering controls of pore-pressure evolution on sediment bed erosion by debris flows," Geophys. Res. Lett. **51**, e2024GL108583, https://doi.org/10.1029/2024GL108583 (2024).
Zhou, G. G. D., Chen, L. L., Mu, Q. Y., Cui, K. F. E., and Song, D. R., "Effects of water content on the shear behavior and critical state of glacial till in Tianmo Gully of Tibet, China," J. Mt. Sci. **16**, 1743–1759 (2019).
Zhou, G., G. D., Cui, K. F. E., Cui, L., Jing, A., Mangeney, Y., Cui, Y. Huang, and X. Chen,, "Segregation-induced flow transitions in rock-ice mixtures: Implications for rock-ice avalanche dynamics," J. Geophys. Res. **129**, e2024JF007831, https://doi.org/10.1029/2024JF007831 (2024).
Zhu, Y. J., Jiang, Y. J., Liu, Y. T., Xie, Q. J., Hu, X. B., and Xia, X., "Material characteristic-controlled particle segregation in rock-ice avalanche," Comput. Geotech. **171**, 106367 (2024).